Correspondence to:

J. Matzka,
juergen.matzka@gfz-potsdam.de

The Geomagnetic *Kp* Index and Derived Indices of Geomagnetic Activity

J. Matzka[1] , C. Stolle[1,2] , Y. Yamazaki[1] , O. Bronkalla[1], and A. Morschhauser[1]

[1]GFZ German Research Centre for Geosciences, Potsdam, Germany, [2]Faculty of Science, University of Potsdam, Potsdam, Germany

Abstract The geomagnetic *Kp* index is one of the most extensively used indices of geomagnetic activity, both for scientific and operational purposes. This article reviews the properties of the *Kp* index and provides a reference for users of the *Kp* index and associated data products as derived and distributed by the GFZ German Research Centre for Geosciences. The near real-time production of the nowcast *Kp* index is of particular interest for space weather services and here we describe and evaluate its current setup.

1. Introduction

Geomagnetic variation consists of quiet variation, which is regular in appearance and mostly of solar electromagnetic radiation origin, and geomagnetic disturbance, which is irregular in appearance and mostly driven by the solar wind. The purpose of the *Kp* index, or *Kp* for short, is to monitor subauroral geomagnetic disturbance on a global scale.

Bartels (1949) introduced the standardized *Ks* and the planetary *Kp* indices (see also Bartels, 1957a, 1957b; Siebert & Meyer, 1996), which are derived from observatory-specific three-hourly *K* indices (Bartels, 1938, 1939; Bartels et al., 1939, 1940). The methodology to determine *Ks* and *Kp* indices is based on earlier indices, namely the global *Km* index (Bartels et al., 1939) and the reduced *Kr* and global *Kw* indices (Bartels et al., 1940). The *K* index, for which Bartels et al. (1939) is an early and excellent description in English, is defined as a quasi-logarithmic measure, ranging in steps of 1 from 0 to 9, of the range of geomagnetic disturbance at a geomagnetic observatory in a three-hourly UT interval (00–03, 03–06, ..., 21–24). Geomagnetic disturbance is also denoted as *K*-variation. The concept of *K*-variation, also referred to as geomagnetic activity or disturbance, predates the discovery of the solar wind and historically, *K*-variation was seen as the effect of 'solar particle radiation' (e.g. Bartels, 1957a). Siebert (1971) and Siebert and Meyer (1996) use this definition: "*K*-variations are all irregular disturbances of the geomagnetic field caused by solar particle radiation within the 3 h interval concerned. All other regular and irregular disturbances are non-*K*-variations. Geomagnetic activity is the occurrence of *K*-variations." We regard geomagnetic disturbance that is instantaneously driven by the solar wind as *K*-variation.

The sum of the *K*-variation and its counterpart, the non-*K*-variation, equals the measured geomagnetic field variation at a geomagnetic observatory. *K*-variation includes geomagnetic pulsations, bays or substorms, sudden commencements, geomagnetic storms (with the exception of the recovery phase, see below) and other geomagnetic disturbance from fast changes in the ring-current and other magnetospheric and ionospheric currents. The non-*K*-variation includes phenomena related to energetic electromagnetic solar radiation (EUV, X-ray) like the daily solar and lunar quiet variation (Bartels & Johnston, 1939; Yamazaki & Maute, 2017) and the rare solar flare effects (SFE; Curto & Gaya-Piqué, 2009; Veldkamp & van Sabben, 1960). However, some phenomena that are related to the solar wind also contribute to the non-*K*-variation because of their regular appearance. Examples are the quiet-time magnetospheric fields of the tail current, the magnetopause current and the ring current that appear as diurnal variation of the geomagnetic field at a point rotating with the Earth (e.g., Maus & Lühr, 2005). Another example is the slow decay of the ring current field in the recovery phase of a geomagnetic storm (e.g., Kamide & Maltsev, 2007). While the ring current field is driven by the solar wind, its decay in the recovery phase is a non-*K*-variation because it is regular in appearance (Menvielle & Berthelier, 1991) and it occurs delayed to the solar wind variation that caused the geomagnetic storm (Siebert, 1971). The slow field change due to geomagnetic secular variation

is also a non-*K*-variation. The non-*K*-variation with the exception of SFEs is longer in period than the *K*-variations (basically exceeding three hours) and can be regarded collectively as the quiet curve. In the presence of *K*-variation, i.e., geomagnetic disturbance, the quiet curve can only be estimated.

The dependence of *K*-variation on geomagnetic latitude is already accounted for in the *K*-indices. Subsequent standardization from *K* to *Ks* further accounts for local time and some minor seasonal effects, but retains the seasonal dependence of energy input from the solar wind to the ionosphere through the magnetosphere (e.g., Siebert & Meyer, 1996). The *Kp* index, ranging from 0 to 9 and given in units of thirds, is the mean of the *Ks* indices of 13 contributing geomagnetic observatories at subauroral latitudes, the so-called *Kp*-stations.

Kp is suitable to parametrize empirical geospace models as it is related to numerous phenomena and it correlates with many parameters in near-Earth space. These include the magnetospheric magnetic field geometry and strength (Tsyganenko, 1989), electron and ion fluxes at geosynchronous orbit, where tail plasma sheet particles can get access to the inner magnetosphere (e.g., Denton et al., 2015; Korth et al., 1999), magnetospheric electric field geometry and strength in the equatorial plane (e.g., McIlwain, 1986), lower band chorus/VLF wave activity (e.g., Agapitov et al., 2015; Shprits et al., 2007) and ultra low frequency (ULF) wave activity (e.g., Ozeke et al., 2014) with its implication for radiation belt dynamics, position of the plasmapause (Heilig & Lühr, 2013; O'Brian & Moldwin, 2003), cold plasma density distribution in the plasmasphere (e.g., Zhelavskaya et al., 2017), ionospheric ion outflow (e.g., Yau et al., 2011), thermospheric density (e.g., Bruinsma, 2015; Emmert & Picone, 2010; Emmert et al., 2020), thermospheric winds (e.g., Emmert et al., 2008), auroral particle precipitation, energy flux and hemispheric power (e.g., Emery et al., 2008; Zhang & Paxton, 2008), global patterns of height-integrated auroral Hall and Pedersen conductivities (e.g., Hardy et al., 1987) and of auroral field-aligned currents (e.g., Workayehu et al., 2019), or the poleward and equatorward auroral boundary location (e.g., Thomsen, 2004; Xiong et al., 2014). Thomsen (2004) relates the *Kp* index to the solar wind through the movement of equatorward edge of auroral precipitation, which relates to the movement of the earthward edge of the tail plasma sheet, which again relates to the magnetospheric convection electric field.

Kp is also important for physics-based geospace models. Examples for magnetosphere/plasmasphere modeling are the VERB-3D model (Subbotin et al., 2011) of the outer radiation belt that has a wave model driven by *Kp*; the 3-dimensional, kinetic model of ring current evolution by Jordanova et al. (2006); and the model of dynamic plasmaspheric density by Pierrard and Stegen (2008), and Pierrard et al., (2009). Examples for the application for ionosphere/thermosphere modeling include the thermosphere-ionosphere-electrodynamics general circulation model (TIE-GCM; Qian et al., 2014), which is a model of the Earth's upper atmosphere that uses *Kp* to specify forcing by the convection electric field, by auroral Joule heating and by particle precipitation heating; and the Whole Atmosphere Community Climate Model with thermosphere and ionosphere extension (WACCM-X; Liu et al., 2018), a whole atmosphere model extending from the ground to the upper thermosphere, with a similar parameterization for geomagnetic forcing as TIE-GCM.

Kp, often in combination with other indices, is also used for data selection in, e.g., geomagnetic, ionospheric, thermospheric and magnetospheric studies as well as geomagnetic field modeling (e.g., Kauristie et al., 2017). Also, the *International Quiet and Disturbed Days*, a product we derive from *Kp* on a monthly basis, are important for data selection.

In space weather application, *Kp* is used for the National Oceanic and Atmospheric Administration (NOAA) Geomagnetic Storms or G-scale, ranging from minor (G1) for *Kp* = 5 to extreme (G5) for *Kp* = 9 (www.swpc.noaa.gov). It is also one of the parameters distributed by ESA's Space Situational Awareness Program (http://swe.ssa.esa.int/). Another example for space weather application is the radiation belt forecast system described by Horne et al. (2013), which is based on *Kp* predictions. It covers the outer radiation belt and the slot region between the inner and outer radiation belt and gives radiation risk indices for internal charging of satellites in geostationary and medium Earth orbit. The *Kp* index is also used to describe and predict scintillations in global navigational system signals at high latitudes. These scintillations are due to strong plasma gradients of ionospheric plasma irregularities (e.g., Xiong et al., 2016, 2018). Secan et al. (1997) used *Kp* to describe and forecast the intensity, latitude and local time of irregularities with the Wideband Ionospheric Scintillation Model and *Kp* has high skill and impact to machine learning-based predictions

of high-latitude scintillations (e.g., McGranaghan et al., 2018). Geomagnetic activity affects thermospheric density (e.g., Bruinsma, 2015) and *Kp* plays an outstanding role in low earth orbit space safety and space traffic management (Berger et al., 2020; He et al., 2020). Finally, Boteler (2001) showed a relation between *Kp* and modeled peak electric field magnitudes due to geomagnetically induced currents (GIC).

In more than 70 years since its inception, *Kp* has proven to be an important and reliable index. Still, some limitations exist compared to other, younger geomagnetic indices. For example, the time resolution of *Kp* is lower than for the PC (Polar Cap) and AE (Auroral Electrojet) indices (one minute resolution) or the Dst index with one-hour resolution (e.g., Rangarajan, 1987). Also, *Kp* is capped to a certain value (i.e., 9) for events with extreme geomagnetic disturbance. In this regard, new *Kp*-like but open-ended indices with 30 and 60 min time resolution have been developed as part of the European Union (EU) project Space Weather Atmosphere Models and Indices (SWAMI; Jackson et al., 2020). These indices, which are already available on https://www.gfz-potsdam.de/en/hpo-index/, will be described in a separate paper. Also, *Kp* does not reflect the universal time (UT) dependent variation of geomagnetic disturbance (Bartels, 1940), while the *Kp*-like *am* index contains this information (Mayaud, 1980; Svalgaard, 1976).

Predictions of *Kp* are usually based on solar wind parameters measured at L1 by satellites like ACE or DSCOVR (e.g. Shprits et al., 2019; Wing et al., 2005; Wintoft et al., 2017; Zhelavskaya et al., 2019) or solar wind parameters plus solar X-ray flux (Chakraborty & Morley, 2020).

A nowcast *Kp* is crucial for space weather applications as described above and for space weather monitoring as it warns operational users in near real-time of potential space weather impacts. GFZ German Research Centre for Geosciences (GFZ) has a nowcast system, which will be later described and discussed in comparison to the definitive *Kp* index and the nowcast system by NOAA.

The *Kp* index is available back to 1932 and thus valuable for space climate studies. With the present publication serving as a reference, the *Kp* index and derived products are now distributed with a digital object identifier (DOI; Matzka et al., 2021, data publication) and under the CC BY 4.0 license.

In what follows, we give a first hand account of the current derivation and distribution of the geomagnetic *Kp* index and its derived products (sections 2.1 and 2.3) and its historical development (section 2.4). We demonstrate some of the fundamental properties of *Kp* based on the data from 1932 to 2019 in section 3.1 and investigate the influence of the *Kp*-stations' change in geomagnetic latitude due to secular variation (section 3.2). In section 3.3 we describe the production and properties of the nowcast *Kp* index. Section 4 describes the distribution and license of the index and section 5 gives a summary and conclusion. We mostly use the terms and notation of Bartels (1957a, 1957b). Like him, we use italics for the letters denoting indices, however, we skip the hyphen in the index names (we use, e.g., "*K* index" and "*Kp* index").

2. Derivation of *K*, *Kp* and Related Products

2.1. Derivation of *K*

Note that *K* indices are a standard product of many geomagnetic observatories from all latitudes, while only 13 subauroral observatories contribute with their *K* indices to *Kp*. More details on geomagnetic observatories are given in, e.g., Matzka et al., (2010) or Chulliat et al. (2017). *K* is an observatory specific geomagnetic index defined on the eight three-hourly intervals of the UT day 00–03, 03–06, ..., 21–24 UT (Bartels et al., 1940). *K* is determined from the two horizontal geomagnetic components. Until 1963, also the vertical component Z has been used to derive *K* (see section 2.4 for the history of *K* and *Kp* and changes in their production). Observatories have different configurations to orient the two perpendicular sensors that measure the horizontal geomagnetic variation. With digital data, the geomagnetic field variations along any field component can be easily calculated from any of these configurations, but in the times when photographic recordings were used, typically until the 1980s, the *K* indices had to be determined directly from photographic paper and thus from the field components that were actually recorded. In the XYZ-configuration, the horizontal geomagnetic field variations are recorded in the geomagnetic component X along geographic north and Y along geographic east. The other typical configuration is the HDZ-configuration. Here, the horizontal geomagnetic variations are recorded by sensors that are mounted approximately along
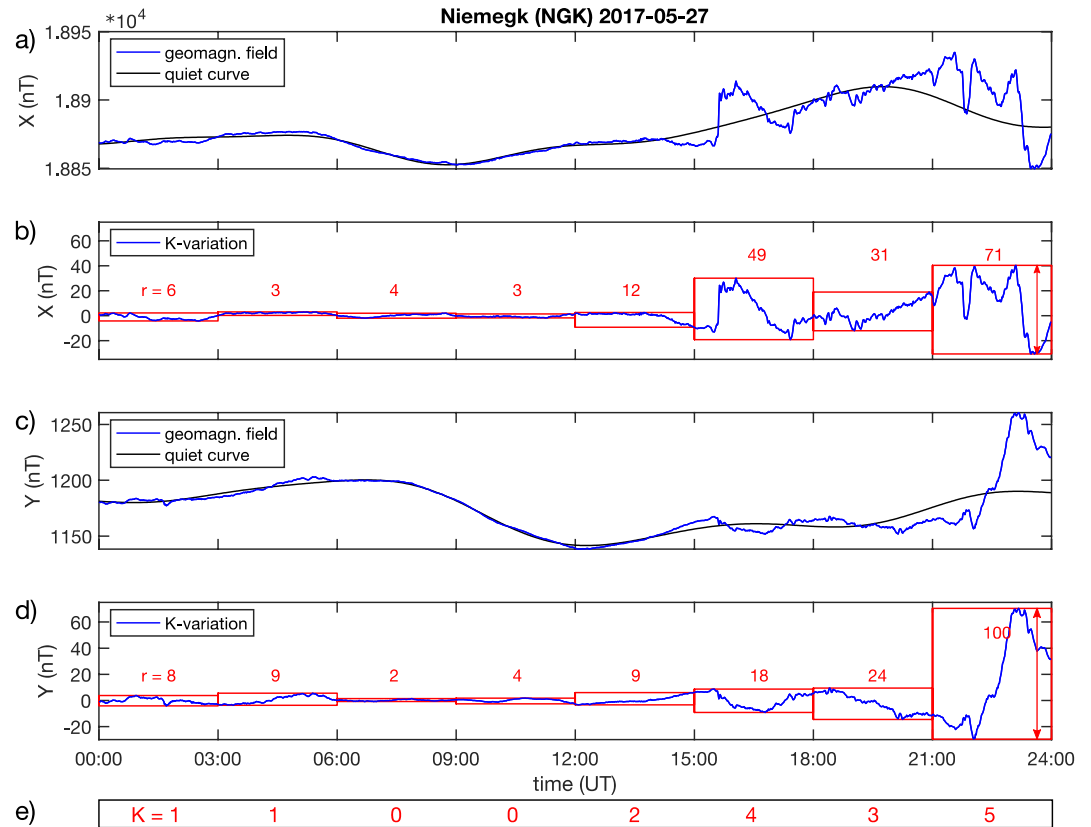
Figure 1. Determining the three-hourly range r of the *K*-variation and the *K* indices for Niemegk on May 27, 2017. (a) X component geomagnetic variation (blue) and non-*K*-variation (quiet curve, black). (b) X component *K*-variation (blue), a red box indicates its maximum and minimum in each three-hour interval. The red numbers on top of each box indicate the corresponding range r in nT, which is also indicated by a vertical arrow for 21:00–24:00 UT. (c) and (d) same as (a) and (b), but for the Y- component. (e) *K* indices for Niemegk for the respective three-hour intervals, as derived from the larger of the corresponding ranges r in panel (b) and (d) according to Table 1.

local magnetic north (as an approximation for the variations of the horizontal field strength, H), and local magnetic east (as an approximation for the variations, in nT, of the geomagnetic declination).

K is derived by first estimating the quiet curve (black curve in Figures 1a and 1c) for each of the two horizontal geomagnetic components (blue in Figures 1a and 1c) at a geomagnetic observatory. In the absence of an SFE (regarding SFEs, see section 2.4.2), the quiet curve is a good representation of the non-*K*-variation and subtracting it from the geomagnetic variations yields the *K*-variation (blue curve in Figures 1b and 1d). Various algorithms exist to estimate the quiet curve and individual observatories made different choices regarding algorithms (see section 2.4.3 for more details on the determination of the quiet curve). The *K*-variation's range r (in nT, that is the same that was labeled "*a*" by Bartels), i.e., the absolute value of the difference between the K-variation's maximum and minimum, is determined separately for each three-hourly interval and for each horizontal component. In Figures 1b and 1d the red box indicates the maximum and minimum for each interval and the value of range r is given by the red number at each red box. Additionally, a double-headed vertical arrow indicates the range r in the interval 21–24 UT.

In each three-hour interval, the *K* index is determined by the horizontal component with the larger range r by converting r to *K* (panel e in Figure 1) according to an observatory-specific scale of lower range-limits, also called the range-limits, or denoted here as the *K*-limits, or individually as the *K*0- (for *K* = 0) to *K*9-limit (for *K* = 9). Table 1 lists the *K*-limits chosen for Niemegk (Bartels, 1938), which is regarded as the standard observatory for *K* indices (Bartels et al., 1939). For example, the range r with 40 nT ≤ r < 70 nT will be assigned *K* = 4 and the *K*9-limit is 500 nT. Additionally, Table 1 shows the frequency distribution of Niemegk's *K* indices and of the single-digit *Kp* indices (see section 2.2) for 1932–2019.

Table 1
K-Limits and Frequency Distribution of K for Niemegk and of Kp

K	0	1	2	3	4	5	6	7	8	9
K-limit[a] [nT]	0	5	10	20	40	70	120	200	330	500
Freq. K [%] for 1938[b]	11.91	25.00	25.44	20.51	10.10	5.10	1.301	0.377	0.171	0.068
Freq. K [%], 1932–2020	7.116	24.42	29.42	23.15	10.62	4.062	0.966	0.188	0.041	0.019
Freq. Kp [%], 1932–2020[c]	10.72	26.31	25.14	19.70	10.97	4.686	1.622	0.573	0.229	0.052

[a]e.g., Bartels et al. (1939). [b]from Bartels et al., (1939). [c]Frequency single-digit *Kp*, see section 2.2.

Bartels et al. (1939) were pleased by the *K*-limit scale chosen for Niemegk because the intermediate values $K = 2$, 3, and 4 occur in the majority of cases (>50%) and both lowest ($K = 0$ and 1) and higher degrees of disturbance ($K > 4$) are distinguished well. This frequency distribution is still well maintained for *K* at Niemegk and for *Kp* for 1932–2019, see Table 1.

By definition, the *K*-limit scales for all observatories are proportional to the Niemegk scale (Table 1). The scales are referred to as quasi-logarithmic (Bartels, 1957b). They start with the *K*0-limit of 0 nT, then *K*-limits are doubling from $K = 1$ up to $K = 4$ in the logarithmic part of the scale, and increase less steeply for $K > 4$. The *K*1-limit is a hundredth of the *K*9-limit. Bartels et al. (1939) determined the individual *K*9-limits of other observatories such that their frequency distribution of *K* values is closest to that of Niemegk. Practically, this was achieved by choosing the *K*5-limit such that the frequency of $K \geq 5$ for any observatory is closest to that of Niemegk, which is slightly more than 5% (Table 1). According to Bartels (1957a, 1957b), only scales with certain *K*9-limits, namely 300 (for equatorial observatories), 350, 500, 600, 750, 1,000, 1,200, 1,500, and 2,000 nT, should be used, but not all observatories adhered to this rule and some adopted scales based on other *K*9-limits. In general, the observatory specific scales are strongly dependent on corrected geomagnetic latitude, or more specifically, on the latitudinal distance to the auroral zone (Mayaud, 1980) and from the 1960s Mayaud used the relationship between *K*9-limit and auroral distance to assign *K*9-limits to geomagnetic observatories.

The derivation scheme for *K* comes with some degree of ambiguity and approximation, e.g., by using geomagnetic recordings in the XYZ-configuration or HDZ-configuration, by using photographic recordings or digital data of various time resolutions, by the estimation of the quiet curve, or by the choice for pre-defined discrete levels of *K*9-limits. This requires extra precaution at a geomagnetic observatory to maintain the reproducibility and homogeneity of its *K* index time series. Any change in procedure at a specific observatory needs to be checked for consistency of results, typically by employing the old and the new procedure in parallel for a certain period of time. Certain aspects of changes are discussed in section 2.4.

The three-hourly ranges and consequently the *K* indices are local time dependent (with a maximum in geomagnetic disturbance around local midnight) and thus the mean frequency distribution of *K* indices is different for the eight intervals of the day (Bartels, 1949; Bartels et al., 1940). The frequency distribution of *K* values is also station dependent.

2.2. Definitive *Kp*, *ap* and *Ap*

Kp is currently derived from 13 contributing geomagnetic observatories, the *Kp*-stations shown in the upper panels of Figure 2. Table 2 gives the current *Kp*-stations together with their operating institutes, the year when they became *Kp*-station, their geographic longitudes and quasi-dipole (QD) latitudes, their *K*9-limits and respective weight in *Kp*. QD coordinates were calculated using IGRF-13 (Alken et al., 2021) and the Fortran code provided by Emmert et al., 2010. The results depend on the maximum degree and order *L* of the spherical harmonic expansion, and the maximum degree *N* of the vertical polynomial expansion. Here, we have used $L = 6$ and $N = 8$. The QD coordinates (Emmert et al., 2010; Laundal & Richmond, 2017) for the *Kp*-stations are almost identical to corrected geomagnetic (CGM) coordinates (Gustafsson et al., 1992) used in many earlier studies.
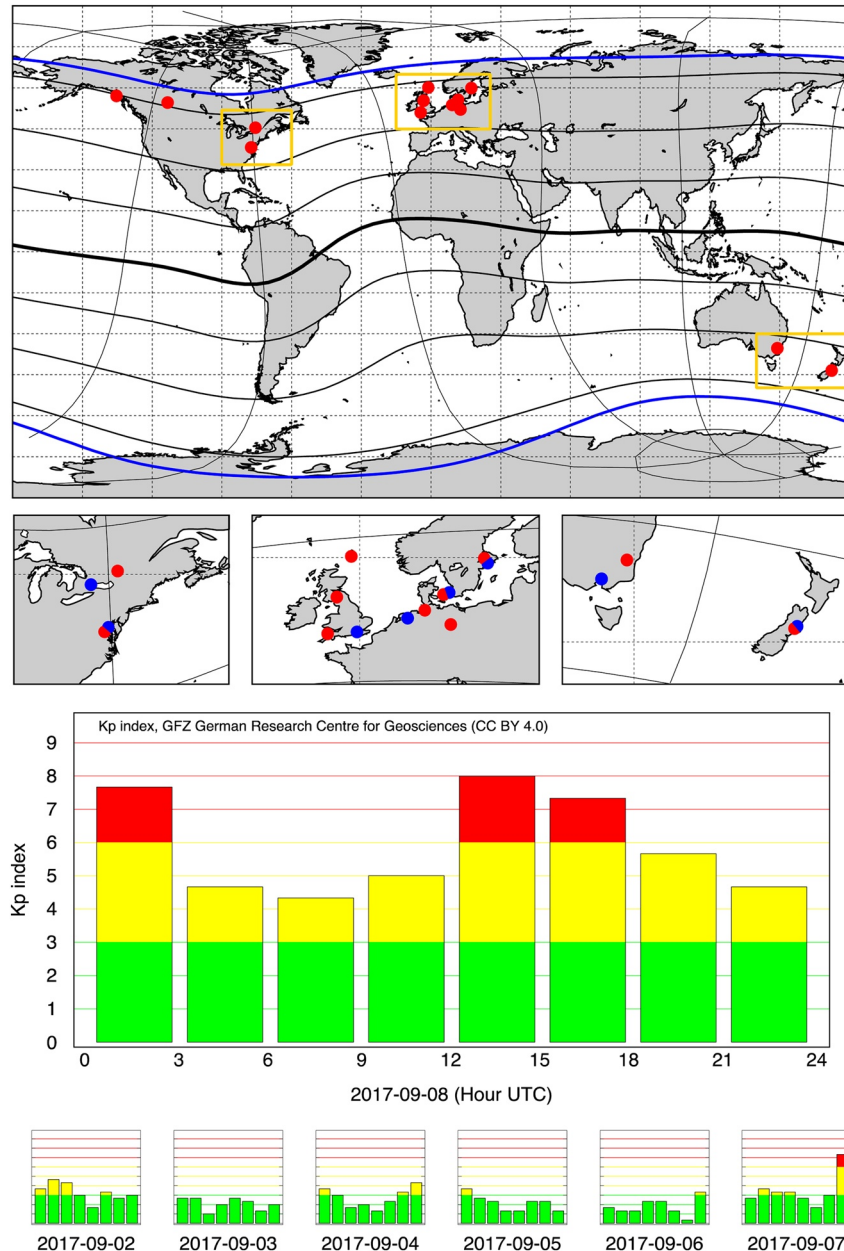
Figure 2. Upper panels: World map of the 13 current *Kp*-stations (red dots, see also Table 2) with geographic coordinates (dotted lines), QD coordinates (solid lines), geomagnetic equator (thick line at 0° QD latitude) and auroral zones (blue lines at +67° and −67° QD latitude). Yellow rectangles indicate the area of the three enlarged regional maps with current (red) and all previous (blue) *Kp*-stations (see section 2.4.4). Lower panels: *Kp* index for September 8, 2017 (top) and the preceding six days (bottom row). Plots of this type are provided for all days since 1932 (see section 4). QD, quasi-dipole.

Like others (e.g., Kauristie et al., 2017; Takahashi et al., 2001; Thomsen, 2004), we regard all *Kp*-stations as subauroral. We note, however, that the subauroral latitudinal range is not clearly defined and depends on the phenomena under investigation and various ranges have been given from, e.g., 40°–55° CGM latitude (Mayaud, 1980) to, e.g., 60°–65° dipole latitude (Oguti, 1993). The choice of subauroral latitudes for the *Kp*-stations is not only crucial for the scientific meaning of the index, e.g., as a proxy for magnetospheric convection (Thomsen, 2004), it also comes with technical advantages for the index production. The separation of *K*- and non-*K*-variation is clearer at subauroral than at lower latitudes because, first, the auroral *K*-variations are more distinct, second, the quiet curve is easier to predict (for the northern component it

Table 2
Geomagnetic Observatories Currently Contributing to Kp (Kp-Stations)

IAGA code	Observatory, institute Abbr.[a], country code	Since year	Geogr. long. [°]	QD lat.[b] [°]	K9-limit [nT]	Weight in *Kp*
EYR	Eyrewell, GNS, NZ	1978	172.4	−49.9	500	0.5
CNB	Canberra, GA, AU	1981	149.0	−45.0	450	0.5
UPS	Uppsala, SGU, SE	2004	17.4	56.6	600	0.5
BFE	Brorfelde, DTU, DK	1984	11.7	51.9	600	0.5
WNG	Wingst, GFZ, DE	1938	9.1	49.8	500	1
NGK	Niemegk, GFZ, DE	1988	12.7	47.9	500	1
LER	Lerwick, BGS, GB	1932	358.8	57.5	1000	1
ESK	Eskdalemuir, BGS, GB	1932	356.8	52.1	750	1
HAD	Hartland, BGS, GB	1957	355.5	46.9	500	1
OTT	Ottawa, NRCan, CA	1969	284.5	54.0	750	1
FRD	Fredricksberg, USGS, US	1957	282.6	47.2	500	1
MEA	Meanook, NRCan, CA	1932	246.7	61.2	1500	1
SIT	Sitka, USGS, US	1932	224.7	59.4	1000	1

[a]BGS, British Geological Survey; DTU, Technical University of Denmark; GA, Geoscience Australia; GFZ, GFZ German Research Center for Geosciences; GNS, GNS Science; NRCan, Natural Resources Canada; SGU, Geological Survey of Sweden; USGS, United States Geological Survey. [b]For 2020, after Emmert et al. (2010).

has less day-to-day variability since it lies further away from the mid-latitude Sq foci), and third, during the main phase of a geomagnetic storm, the ionospheric auroral *K*-variations dominate the ring current signal, which is a non-*K*-variation. Using measurements at subauroral latitudes also has advantages over the data from auroral latitudes. At auroral stations, the *K*-variation is mostly of local ionospheric polar electrojet origin (and predominantly in the northern horizontal component, which then determines the *K* index). At subauroral stations, *K*-variation from large scale ionosphere-magnetosphere current systems (e.g., McPherron & Chu, 2017) play an important role (and show up, with comparable range, in both the northern and eastern horizontal component). Therefore, *K* indices from subauroral stations are sensitive to a much larger current system and broader longitudinal sector of the auroral oval than *K* indices from auroral stations and hence depend less on regional scale geomagnetic activity, see p. 29 in Mayaud (1980). Consequently, it is expected that the global geomagnetic activity level can be gauged by a smaller number of subauroral stations than would be required from auroral stations. At the same time, the subauroral latitudes are more suitable to magnetically monitor the equatorward auroral oval expansion during strong storms as the auroral oval moves away from the auroral stations, which might see a concurrent decrease in *K*-variation.

The definitive *Kp* index is derived from the *K* indices of the *Kp*-stations, which are sent to the Adolf-Schmidt-Observatory for Geomagnetism Niemegk on a semimonthly basis. There, the *K* indices are converted to standardized *Ks* indices by using conversion tables. Following Bartels (1949), in these tables, integer values from 0 to 27 are given for each possible value of *K* for each UT three-hour interval and Lloyd season (see Table S1, including a short description of their use). The three Lloyd seasons are equinoxes (March, April, September, October (MASO)), June solstice (May, June, July, August (MJJA)) and December solstice (November, December, January, February (JFND)). The integer values 0 to 27 represent 3*Ks. Dividing 3*Ks by 3 gives *Ks*, an index expressed on a scale of thirds ranging from 0 to 9. Bartels (1949) determined the conversion tables such that the frequency distribution of the *Ks* values for each *Kp*-station and in each three-hour interval of the UT day best resembles the so-called standardizing distribution. This standardizing distribution corresponds to the frequency distribution, averaged over all *Kp*-stations, of the *K* indices in the two UT intervals closest to local midnight and in the respective Lloyd season. Deviating from this principle, *K* = 0 is always assigned 3*Ks = 0 and *K* = 9 is always assigned 3*Ks = 27. Conversion tables exist for each Lloyd season (JFND, MASO, MJJA) to account for the seasonal change of the local time dependence of *K*. At the season boundaries, the seasonal change is smoothed with the help of transition tables (Table 10 in

Table 3
Definitive Kp, 3*Kp, ap and Their Frequency Distribution from 1932 to 2019

Kp	0o	0+	1−	1o	1+	2−	2o
3*Kp	0	1	2	3	4	5	6
ap[a] [2 nT[b]]	0	2	3	4	5	6	7
Freq.[c] [%]	3.55	7.17	8.58	8.87	8.85	8.62	8.49
Kp	**2+**	**3−**	**3o**	**3+**	**4−**	**4o**	**4+**
3*Kp	7	8	9	10	11	12	13
ap[a] [2 nT[b]]	9	12	15	18	22	27	32
Freq.[c] [%]	8.03	7.40	6.56	5.74	4.59	3.68	2.71
Kp	**5−**	**5o**	**5+**	**6−**	**6o**	**6+**	**7−**
3*Kp	14	15	16	17	18	19	20
ap[a] [2 nT[b]]	39	48	56	67	80	94	111
Freq.[c] [%]	2.13	1.47	1.09	0.739	0.522	0.361	0.261
Kp	**7o**	**7+**	**8−**	**8o**	**8+**	**9−**	**9o**
3*Kp	21	22	23	24	25	26	27
ap[a] [2 nT[b]]	132	154	179	207	236	300	400
Freq.[c] [%]	0.178	0.133	0.105	0.065	0.059	0.041	0.011

[a]After Bartels et al. (1957b). [b]Siebert (1971) recommends to regard ap as dimension-less index and to ignore the unit of 2 nT. [c]Frequency distribution 1932–2019.

Bartels, 1949). Additionally, $K = 0$ around midnight was found to be less frequent in summer (MJJA in the northern hemisphere, JFND in the southern hemisphere) than in winter. Combined with the larger number of Kp-stations in the northern hemisphere, this would lead to an artificial seasonal variation. This artificial seasonal variation is compensated in Kp (Bartels, 1949) through the conversion tables for MJJA (note that for $K = 1$ and 2 the values for 3*Ks are smaller for MJJA than for JFND). Also, on purpose, no 3*Ks value appears twice in the conversion tables within any eighth of the UT-day for any observatory, allowing K to be reconstructed unambiguously from Ks. The average 3*Ks of Eyrewell and Canberra as well as of Uppsala and Brorfelde count as one Kp-station each (weight in Table 2). The average of 3*Ks for a specific three-hour interval is rounded to the integer 3*Kp, i.e., three times the Kp index. Figure 2 (lower panels) shows, as an example, the Kp index for the geomagnetic storm on September 7 and 8, 2017, and preceding days.

The definitive Kp index as described in the previous paragraph is endorsed by the International Association of Geomagnetism and Aeronomy (IAGA). It is available back to 1932. Kp is a global index of geomagnetic activity for each three-hour interval of the UT day. It is traditionally represented by either 3*Kp = 0, 1, …,27, or in symbol notation by Kp = 0o, 0+, 1−, 1o, 1+, …, 9−, 9, where o, + and − represent the integer (o), plus one third (+) and minus one third (−), respectively. Sometimes, Kp is represented as Kp = 0, 0.3, 0.7, 1.0, 1.3, …, 8.7, 9.0 (or without decimal points: 0, 03, 07, 10, 13, …, 87, 90), and one must not misinterpret these as direct numerical values (e.g., 0.3 is not identical to one third). A traditional graphical way to represent Kp is the so-called note-script or musical diagram (Bartels, 1949), which is organized according to Bartels solar rotation and is available back to 1932 (see section 4. and an example in Figure S1). Kp may sometimes also be rounded to a single-digit integer number and presented with reduced resolution as 0, 1, …9. Examples for the use of the single-digit Kp are the comparison of the frequency distribution of Kp with that of K at Niemegk in Table 1.

Kp with its underlying quasi-logarithmic scale does not lend itself for the calculation of arithmetic means (e.g., daily means, yearly means). To this end, Kp is converted to the linear ap, the three-hourly equivalent planetary amplitude according to Table 3. Sometimes, and to a certain degree confusingly, ap is assigned a unit of 2 nT, sometimes it is regarded as an index without units (Siebert, 1971). By multiplying the numerical value of ap by 2 nT, the average range in nT of the geomagnetic disturbance at a Kp-standard station (located, like Niemegk, at about 50° geomagnetic latitude, with K9-limit = 500 nT) is obtained. For example,

we have $ap = 80$ for $Kp = 6$ (see Table 3) and $80*2$ nT = 160 nT is the mean disturbance range for $K = 6$ at Niemegk (120 nT $\leq r < 200$ nT, see Table 1). The average (arithmetic mean) of the eight ap indices of a UT day rounded to an integer is the daily equivalent planetary amplitude Ap (again in units of 2 nT, or dimensionless). Monthly and yearly means of ap have also been labeled "monthly Ap" and "yearly Ap".

2.3. Derived Products *Cp*, *C*9, and International Quiet and Disturbed Days

The planetary international magnetic character figure Ci is an index predating Kp and not in use anymore. Based on the daily sum of ap, which has a higher numerical resolution than the rounded Ap values, for each UT day, a planetary geomagnetic index $Cp = 0.0, 0.1, ...$ to 2.5 is derived that replaces the earlier Ci index (for details, see Mayaud, 1980; Rangarajan, 1987). Cp is still a standard product and we publish it along Kp in some data products. The Cp index can be contracted to the single digit integer index $C9$. Tables to convert the daily sum of ap to Cp and $C9$ are given by Bartels (1957b) and in Tables S2 and S3. The so-called R9C9-plots (Figure 4 in Siebert & Meyer, 1996) showed both $C9$ and the three-day mean sunspot number and are now replaced by SN9C9-plots to reflect the change in the sunspot number series in 2015 (Clette and Lefèvre, 2016), see section 4). The SN9C9-plots allow direct graphical comparison of sunspot number and $C9$, ordered according to solar rotations (also available back to 1932, see section 4. and an example in Figure S2).

The *International Quiet and Disturbed Days* are determined from Kp on a monthly basis. For each month, days are ordered according to the daily Kp sum, the daily sum of the square of Kp, and the largest Kp of the day (Bartels, 1957b). The days in the ordered sequences are then numbered and for each day the mean of the three numbers is a measure of its relative geomagnetic activity within this month. The month's 10 most quiet days and the 5 most disturbed days according to this mean are published by GFZ as the *International Quiet and Disturbed Days* (see section 4). They are available back to 1932. The list of *International Quiet and Disturbed Days* is often applied to identify geomagnetically quiet or disturbed periods for geomagnetic and space physics studies.

2.4. Historical Development of *Kp*

The previous sections describe the current definitive Kp index production. Here, we describe historical changes to the Kp index and to the rules for its production.

2.4.1. Associations and Institutions Involved

The K index was adopted in 1939 by the International Association for Terrestrial Magnetism and Electricity (IATME), the predecessor of IAGA. Until 1948, observatories reported K indices to the U. S. Coast and Geodetic Survey or the Department of Terrestrial Magnetism, Carnegie Institution of Washington. From 1949 onward, K indices were reported to the C + K-Center at Koninklijk Nederlands Meteorologisch Instituut, De Bilt, Netherlands (see Journal of Geophysical Research 54, 1949, p. 196). The Center was later renamed to Permanent Service of Geomagnetic Indices (PSGI) and International Service of Geomagnetic Indices (ISGI). K indices were published in IAGA bulletins until 1969 and thereafter by the World Data Centres (WDC; Siebert & Meyer, 1996). K values from 1957 to 1997 are archived at WDC Copenhagen in analog form. Today they are collected digitally by INTERMAGNET (St-Louis, 2012). ISGI is a service of IAGA and is now hosted by University Strasbourg, École et Observatoire des Sciences de la Terre (EOST). Kp was produced at University of Göttingen from 1949 to 1996. In 1997, the responsibility for producing Kp was given to GFZ German Research Center for Geosciences, Adolf-Schmidt-Observatory for Geomagnetism Niemegk, Germany, which at the same time became an ISGI Collaborating Institute. Kp is an IAGA-endorsed index since 1954.

2.4.2. Changes of Rules Affecting *K* and *Kp*

Until 1963, the K indices were determined from the geomagnetic disturbance in all three components. However, geomagnetic induction (e.g., Kuvshinov, 2008) enhances the variation of the horizontal components and decreases the variation of the vertical component Z. And since only the component with the largest range determines the K index, the Z component is not expected to play a role for K except for stations in close proximity to the auroral electrojet and for stations with anomalous subsurface induction effects

(Siebert, 1971). Induction also smoothens the variation in the Z-component, making it more difficult to separate *K*-variation from non-*K*-variation in Z (Mayaud, 1980). IAGA resolution 4 from 1963 determined "...that from the 1st of January 1964, the Z-component will not be used for the measure of the three-hourly K-index, except by the standard Kp-observatories, ...". The advent of computer-derived *Kp* indices and its implication for the *Kp*-stations in this context will be discussed in section 2.4.3.

SFEs can be difficult to identify in magnetograms even for experienced observers and hence, from 1968 onwards (according to IAGA resolution 12 in 1967), the *K* and *Kp* indices should include SFE's as *K*-variation instead of treating them as a non-*K*-variation. This simplified the production of *K* and *Kp* (also for the later introduced computer algorithms, see section 2.4.3), and has little practical influence on the *Kp* series due to the very rare occurrence of SFEs. For time intervals affected by an SFE, an additional *K′* and *Kp′* index should be determined that treats SFE's as non-*K*-variation. *K′* and *Kp′* should be published supplementary to *Kp*. Note that the same instruction was already published 10 years earlier by Bartels (1957a). Note also that there currently is a lack of procedures for collecting *K′* as well as for distributing and archiving *Kp′*. This should be addressed in the future.

2.4.3. Introduction of Algorithm-Derived *K* Indices

The most complex task in deriving *K* indices is estimating the non-*K*-variation (or quiet curve) in order to determine its counter-part, the *K*-variation (or geomagnetic disturbance). Since Sq has a significant day-to-day variability, estimating the quiet curve for hand-scaled *K* indices required experienced personnel familiar with the typical geomagnetic variation at a station. More than 95% of the *K* indices obtained independently by two persons would typically be identical and any differences in the derived *K* indices would be randomly distributed and never exceed one unit (Menvielle, 1981; Rangarajan, 1987). Experienced persons that are hand-scaling *K* indices for observatories with which they are not personally familiar would achieve 92% identical results when excluding ranges *r* close to a *K*-limit, and 80%–85% including the cases with ranges *r* close to a *K*-limit. It was argued that the difference between algorithm-derived *K* indices and hand-scaled *K* indices should not be larger than the typical difference between independently hand-scaled *K* indices. Based on one year of data from 10 subauroral and 1 auroral observatory, IAGA finally endorsed four algorithms that achieved at least 69.9% accordance to hand-scaled *K* indices, with differences in derived *K* indices greater than one amounting to less than 2% (Menvielle et al., 1995). The four endorsed algorithms are the Adaptive Smoothing Method (ASM; Nowozynski et al., 1991), Finnish Meteorological Institute method (FMI; Sucksdorff et al., 1991), linear-phase robust non-linear smoothing (LRNS; Hattingh et al., 1989) and United States Geological Survey method (USGS; Wilson, 1987). The algorithms in use today at the various *Kp*-stations are FMI (for observatories NGK, UPS, WNG), semiautomatic LRNS (for CNB), USGS (for FRD, SIT), two modified ASM algorithms of which one is BGS (for HAD, ESK, LER) described in Clark (1992) and the other one is used for MEA and OTT, and additionally the NZ algorithm (McNoe, 1989) for EYR. Geomagnetic observatories traditionally are very concerned about the homogeneity of their data series and since all these organizations are aware of the importance of their *K* indices, we can assume that the agreement between algorithm-derived and hand-scaled *K* indices was carefully tested at each *Kp*-station. This test is documented in Wilson (1987) for the USGS method and Clark (1992) for the BGS method. The algorithms use one-minute observatory data, typically from several days, which is smoothed to yield the quiet (or smooth) curve for a particular UT day. However, all these algorithms have in common that *K* is determined from the horizontal components alone, and not from the Z component, even for the *Kp*-station closest to the auroral zone. The provision made in IAGA resolution 4 from 1963 that *Kp*-station should continue to produce their *K* indices based on all three components is not any more adhered to with algorithm-derived *K* indices. The effect on *K* and consequently *Kp* should nevertheless be minor (see Section 2.4.2).

2.4.4. Changes to the Network

Some *Kp*-stations had to be replaced for operational reasons. The original 11 *Kp*-stations are Amberley in New Zealand, Witteveen in the Netherlands, Rude Skov in Denmark, Wingst in Germany, Lerwick, Eskdalemuir and Abinger in the UK, Agincourt and Meanook in Canada and Cheltenham and Sitka in the US (Bartels, 1949). All contribute to *Kp* back to 1932 except Wingst, which started in 1938. In 1954, Lovö, Sweden, was added as *Kp*-station and consequently Rude Skov and Lövö have been weighted by 0.5 each. In 1957, Hartland replaced Abinger, and Fredericksburg replaced Cheltenham. In 1969, Ottawa replaced Agincourt. In 1972, Toolangi in Australia joined and Amberley and Toolangi consequently are each weighted

as half a *Kp*-station (Siebert, 1971). Amberley was replaced by Eyrewell in 1978, Toolangi by Canberra in 1981, Rude Skov by Brorfelde in 1984 and Witteveen by Niemegk in 1988 (Siebert & Meyer, 1996). In 2004, Uppsala replaced Lovö as *Kp*-station in Sweden. The current *Kp*-stations are listed in our Table 2 and the current and previous stations are shown in the upper panels of Figure 2.

While Agincourt had a *K*9-limit of 600 nT, Ottawa has a *K*9-limit of 750 nT due to its higher QD latitude. Note that Canberra, which replaced Toolangi (*K*9-limit 500) in 1981, has a *K*9-limit of 450 nT, a value not originally foreseen as *K*9-limit by Bartels (1957a, 1957b). All other replacing (new) *Kp*-stations have the same *K*9-limit as their predecessor station. When *Kp*-stations were replaced, no changes in the calculation of *Ks* from *K* were introduced to compensate for the change in location (Rangarajan, 1987), except for Niemegk replacing Witteveen (see Table S1).

The magnetic field of single-wire, high-voltage DC power lines between Germany and Sweden affect Brorfelde (BFE) observatory since December 1994 (Matzka et al., 2009). The effect on *K* was investigated from December 2008 to February 2009, a period of very low geomagnetic activity with 30% of the *K* values of BFE being 0 (mean Ap < 5, corresponding to Kp < 2-). Errors in *K* derivation due to the power line magnetic field predominantly had the effect of shifting *K* = 0 to *K* = 1. This happened for 13% of the *K* = 0 values or 4% of all *K* values (Fox-Maule et al., 2009). For higher magnetic activity, the rate of *K* = 0 and hence the rate of affected *K* values will decrease. Moreover, since Brorfelde contributes with weight 0.5 to *Kp*, the overall effect on *Kp* is expected to be small.

More information on the current *Kp*-stations is given in Table 2 and the effect of changes to the network will be further addressed in section 3.2.

3. Properties of *Kp* and Nowcast *Kp*

3.1. Fundamental Properties of *Kp*

This section describes basic characteristics of *Kp* and its relation to other solar-terrestrial parameters, which help users understand the temporal behavior of *Kp*. The long-term variation of *Kp* is illustrated in Figure 3a as a time series of annual mean *Kp* values from 1932 to 2019. The annual means were calculated from the linearly scaled *ap* index and then converted back to the equivalent *Kp* values. Also shown in Figure 3a is the total sunspot number for the corresponding period. The sunspot number exhibits the well-known solar cycle with a period of ~11 years. The annual mean *Kp* also shows an 11-year period, but tends to be largest during the declining phase of the solar cycle, i.e., when overall geomagnetic activity is elevated due to long-lasting high speed solar wind streams (Lockwood et al., 1999). It can be noted in Figure 3a that geomagnetic activity was particularly low during the solar minimum year of 2009, which resulted from unusually weak solar wind forcing (Russell et al., 2010).

Kp is strongly connected with some solar wind parameters. Figure 3b shows the dependence of *Kp* on solar wind speed and interplanetary magnetic field (IMF) clock angle. The IMF clock angle is defined as $\theta = \arctan(By/Bz)$, where By and Bz are the eastward and northward components of the IMF, respectively. For $\theta = 0°$, IMF is purely northward in the Y-Z plane in geocentric solar magnetic (GSM) coordinates. Similarly, IMF is purely eastward for $\theta = 90°$, westward for $\theta = -90°$, and southward for $\theta = \pm180°$. We used the OMNI 1-min solar wind data estimated for the Earth's bow shock nose (King & Papitashvili, 2005) for the years 1981–2019. The data were time-shifted by 20 min to take into account the time for solar wind signatures to propagate from the bow shock nose to the ionosphere (Manoj et al., 2008) before being averaged over three-hour intervals and compared with the corresponding *Kp*. As seen in Figure 3b, high *Kp* occurs preferably under southward IMF conditions ($\theta = \pm180°$). This is because the southward IMF can most effectively merge with the Earth's northward magnetic field, which leads to solar wind energy injection into the magnetosphere. As shown in Figure 3b, *Kp* also depends on the solar wind speed, as the merging rate increases with increasing solar wind speed. A comprehensive discussion was presented by Newell et al. (2007) and Kauristie et al. (2017) as to how *Kp* and other geomagnetic indices are related to various solar wind parameters.

Kp variations on intra-seasonal time scales are dominated by the solar rotation effect, which produces a spectral peak around 27 days, as seen on the Lomb-Scargle periodogram in Figure 3c. Depending on the
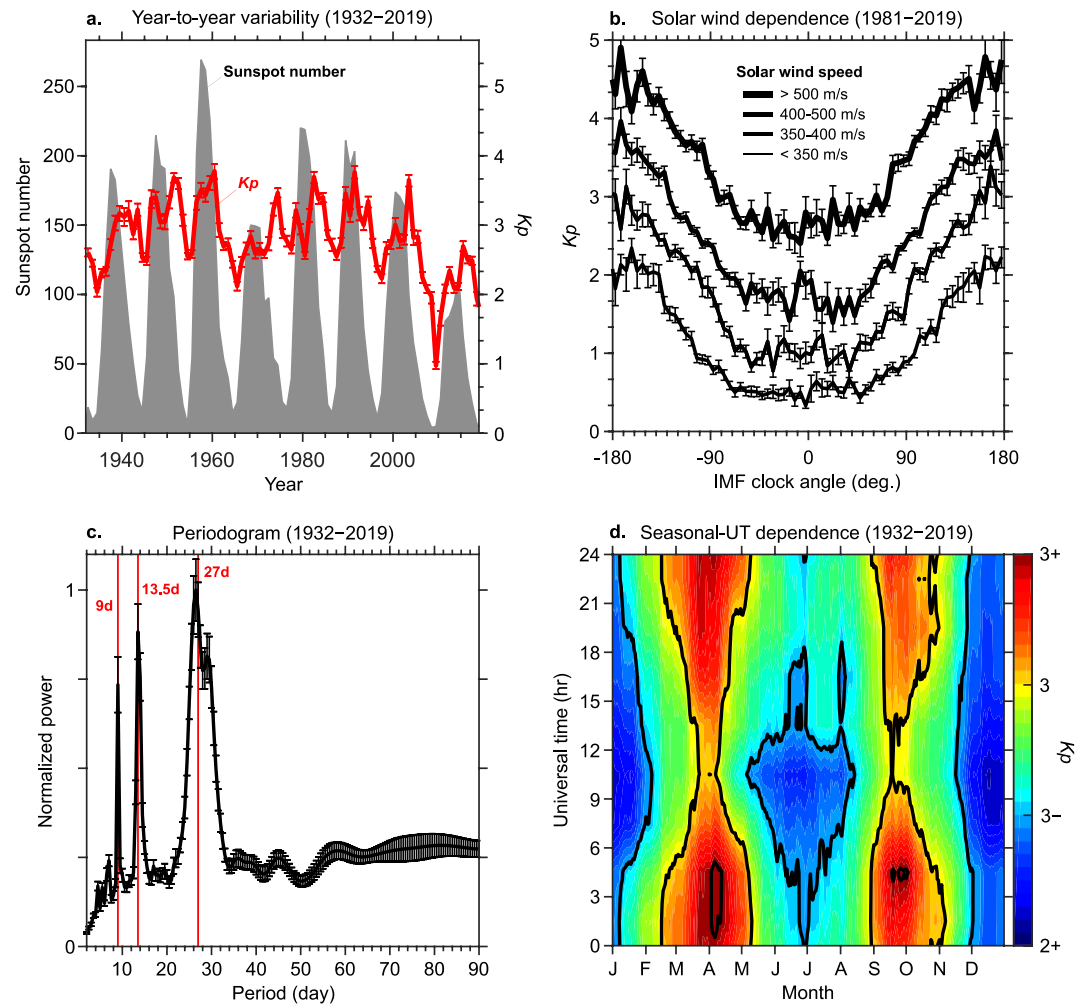
Figure 3. (a) Time series of the annual mean *Kp* values (red) and total sunspot number (gray) during 1932–2019. (b) Dependence of *Kp* on the interplanetary magnetic field (IMF) clock angle and the solar wind speed for 1981–2019. (c) Lomb-Scargle normalized periodogram of *Kp* 1932–2019. (d) Seasonal and universal time (UT) dependence of *Kp* 1932–2019. The error bars in (a), (b) and (c) represent the standard error of the average. In (a), (b) and (d), mean *Kp* values were derived by converting from the corresponding mean values of *ap*.

zonal distribution of active regions of the Sun, spectral peaks also appear at ∼13.5 and ∼9 days. These periodic variations have a significant influence on the weather of the thermosphere and ionosphere e.g., Lei, Thayer, Forbes, Sutton, & Nerem, (2008); Lei, Thayer, Forbes, Wu, et al. (2008).

Local geomagnetic activity and hence *K* indices are known to depend on local time (LT) and season. Averages of *K* indices from a globally well-distributed network of stations should exclude local time influences (Bartels et al., 1939) but might depend on universal time UT due to processes like the daily rotation of the Earth's geomagnetic dipole axis with respect to the Sun-Earth line. The standardization process described in section 2.2 should remove, to a large extent, the UT dependence of *Kp* (Bartels et al., 1940). In fact, the dependence of *Kp* on UT is only one third of a unit (during equinoxes) or smaller (Figure 3d). *Kp*, however, shows a marked seasonal variation with equinoctial maxima (Figure 3d) with an amplitude of about one unit. This is probably due to geomagnetic storms that are more frequent in equinoxes than in solstices (e.g., Cliver et al., 2000; Russell & McPherron, 1973).

Thus, *Kp* contains information both on the solar wind as well as on the coupling between the solar wind and the magnetosphere-ionosphere system (Cliver et al., 2000; Russell & McPherron, 1973; Siebert & Meyer, 1996).
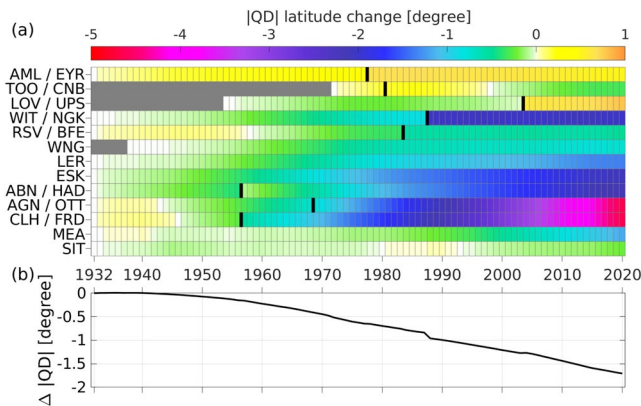
Figure 4. Change in unsigned QD latitude (|QD| latitude) of *Kp*-stations due to secular variation and station replacement. (a) Change of unsigned QD-latitude (color-coded) from 1932 to 2020 for each *Kp*-station (IAGA code indicated on the left). Black bars indicate the eight replacements of stations and IAGA codes for both the replaced and replacing station are given. Gray indicates years for which stations did not contribute to *Kp*. (b) Weighted mean change in unsigned QD latitude of the *Kp*-stations (left). IAGA, International Association of Geomagnetism and Aeronomy; QD, quasi-dipole.

3.2. Distance of the *Kp*-Stations to the Auroral Zone

The average range of geomagnetic disturbance at subauroral latitudes shows a strong dependency on the distance to the auroral zone (e.g., figure 14 in Mayaud, 1980). The smaller the distance to the auroral zone, or the larger the CGM or QD latitude of a subauroral station, the larger is the average range of geomagnetic disturbance or *K*-variation. In *K* and *Kp*, this latitudinal dependency is compensated by a suitable choice of the *K*9-limits (Bartels et al., 1939; Mayaud, 1980). Geomagnetic secular variation and station replacements will change the QD latitude of the *Kp*-stations with time and with it the average range of geomagnetic disturbance. However, once a *K*9-limit is chosen for an observatory, this *K*9-limit usually is not changed any more. This could lead to a bias in the time series of the *Kp*-stations' *K* indices and in *Kp*, which we want to investigate for the period 1932–2020.

First, we investigate the change in QD latitude of the *Kp*-stations due to secular variation and due to the station replacements described in section 2.4.4. Here, we neglect the change in QD latitude arising from the replacement of TOO by CNB and AGN by OTT, assuming that the adapted *K*9-limits (see section 2.4.4) compensate the effect of latitudinal difference on the stations' *K* indices. Likewise, we here do not investigate how the introduction of new *Kp*-stations (i.e., TOO, LOV and WNG) affected *Kp*. In Figure 4a, the change in unsigned QD latitude with time due to secular variation and station replacement is shown color-coded for each of the 13 *Kp*-stations (using unsigned QD latitude makes sure that a poleward change in QD latitude has a positive sign for both the northern and southern hemisphere). The change in QD latitude was strongest (almost −5°) for OTT and FRD in North America.

The *Kp*-stations' weighted (according to their weight in *Kp*) mean change in unsigned QD latitude is plotted in Figure 4b and amounts to −1.7° from 1932 to 2020. The change due to the *Kp*-station replacements amounts to only −0.06°. Thus, stations replacement contributed only negligible and secular variation is the by far dominant process for the mean decrease in the unsigned QD latitude of the *Kp*-stations since 1932.

The auroral zone, i.e., the maximum of aurora sightings, is at around 67° geomagnetic latitude at least since the 19th century (Akasofu, 2003; Chapman & Bartels, 1940; Fritz, 1881) and if the QD latitude of the auroral zone stayed constant since 1932, then the mean decrease by 1.7° in the unsigned QD latitude would be a good estimate for the mean increase in auroral zone distance since 1932. Smith et al. (2017) found that the location of the auroral electrojet has changed from 1970 to 2014 in the same way as the QD latitudes have changed, confirming that the location of the auroral zone remained constant with respect to QD latitude. Changes in the dipole moment of the Earth's magnetic field could also affect the location of the auroral zone, but the observed change in dipole moment from 1932 to 2020, and its relationship to the location of the polar cap boundary (Cnossen et al., 2012), a proxy for the auroral zone location, yield a negligible southward movement of the auroral zone by 0.2°. Hence, the mean distance of the *Kp*-stations' auroral zone distance increased by about 1.7° QD latitude. To estimate the effect on the *Kp* time series of this change in auroral zone distance, we consider Thomsen (2004), who investigated the expansion of the auroral oval due to magnetospheric convection.

Thomsen (2004), based on studies by Gussenhoven et al. (1981, 1983), found a linear relationship between the latitude of the equatorward auroral boundary (the ABI index) and *Kp*. *Kp* decreases by 0.4 units per 1° CGM latitude change of the auroral boundary toward the equator. The CGM latitudes in this range are almost identical to QD latitude and we will use QD latitude here. The relationship is linear and holds for $1 \le Kp \le 7$ (see Figure 1 in Thomsen, 2004). However, the relationship describes the cumulative effect from the intensification of the current systems during auroral expansion on the one hand, and from the change in auroral boundary on the other hand (Thomsen, 2004). The relationship is thus an upper limit for the effect of auroral boundary movement, which is equivalent to decreasing the auroral zone distance to the

Kp-stations. This results in a (negative) bias in the *Kp* series due to a change in auroral zone distance since 1932 of not larger than 1.7°*0.4/° or about two thirds of a unit. In order to get a better estimate of the bias in *Kp*, we now estimate the effect of current intensification during auroral expansion on *Kp* to subtract it from this upper limit.

Smith et al. (2017) investigated the global auroral ovals with magnetic data from satellites in near-Earth orbit. Their study is limited to the auroral electrojet currents for Kp ≤ 4 (but according to Table 3, this accounts for >90% of all *Kp* values) and yields higher QD latitudes for the auroral oval than the electron precipitation data investigated by Thomsen (2004). Smith et al. (2017) suggest (their figure 7) roughly a doubling of the auroral electrojet current strength for an increase in *Kp* by 2 for 0 ≤ *Kp* ≤ 4. For a doubling of the currents, the range of the *K*-variation would double and given the logarithmic scale for *K* ≤ 4, *Kp* would increase by about 1. Hence, about half of the increase in *Kp* comes from current intensification, and the other half is due to the approaching of the auroral oval during expansion. The results by Smith et al. (2017) allow separating the effect of auroral expansion and current intensification. They are about equally strong, but this remains a rough estimate since the auroral electrojet is only one of a number of current systems that affect *K* and *Kp* and while some current systems, like the field-aligned currents associated with the auroral electrojet, vary similarly to the auroral electrojet, others may vary differently. After subtracting this current intensification estimate from the upper limit by Thomsen (2004), our best estimate for the effect of changing auroral zone distance on *Kp* is 0.2 units per ° QD latitude and thus the bias in the *Kp* series since 1932 is in the order of minus one third of a unit, a number that is small compared to, e.g., the year-to-year variability of *Kp* shown in Figure 3a.

This negative bias in the *Kp* series since 1932 is due to the change in auroral oval distance due to secular variation. Other possible effects of secular variation on *Kp*, e.g., a change in geomagnetic declination, are not accounted for here and likely much smaller.

3.3. Nowcast *Kp* at GFZ

As described in section 2.2, the definitive *Kp* index is calculated from the *K* indices derived at each of the *Kp*-stations. Each *Kp*-station sends its *K* indices semimonthly to Niemegk, where the definitive *Kp* index is derived. In parallel, Niemegk also derives the so-called nowcast *K* indices and nowcast *Kp* index directly from near real-time magnetic data provided by the *Kp*-stations. GFZ distributes both the nowcast and the definitive *Kp* index.

At GFZ, the FMI algorithm (FMI stands for Finnish Meteorological Institute, where the algorithm was developed, see Sucksdorff et al., 1991) is used to determine the nowcast *K* values from 1 min data, which is provided by the institutes operating the 13 *Kp*-stations in near real-time (NRT). Data gaps of up to 15 min are linearly interpolated. The NRT data typically arrives with a delay of 5–10 min. Any incoming NRT data as well as any incoming delayed data (e.g., due to data transfer problems) triggers a recalculation of the affected nowcast *K* indices (and consequently the *Kp* index, see next paragraph). In these NRT operations, we calculate the first estimate of the *K* index in the current three-hour interval once 30 min of data (until mid of August 2020: 90 min of data) are available in this interval. At that time, the nowcast *K* reflects only geomagnetic activity that is included in the available data. Therefore, the range of the *K*-variation and consequently the nowcast *K* at this stage can be significantly smaller than the nowcast *K* calculated once all data of the three-hour interval are available (again, the same applies to *Kp*). For all previous intervals, *K* from a specific station is only given if at least 90 min of data are available for this interval. The FMI method estimates the quiet curve of any given UT day from the 1 min data of the previous day, the day itself, and the subsequent day. Therefore, nowcast *K* (and hence *Kp*) values can change with time until all data is available for these three days. To prepare the NRT data for use with the FMI method, we always fill in the missing future observatory data from the current and subsequent day with constant values equal to the latest 1 min data received. Within a three-hour interval, the nowcast *K* indices from the different *Kp*-stations are compared with each other. The largest *K* value is set invalid for the calculation of *Kp* if the difference between the largest and the second largest *K* value exceeds 3 units. This happens very seldom and up to now was caused by erroneous spikes or jumps in the 1 min NRT data resulting in erroneous *K* = 9 values during periods of significantly lower geomagnetic activity.

The first nowcast *Kp* index for an interval is published once the *K* values from at least 5 stations are available, which typically happens 35 min after the start of the three-hour interval. At that time, the nowcast *Kp* reflects only geomagnetic disturbance that is included in the available data and normally its value is significantly smaller than the value obtained when all data within the three-hour interval is available for calculating the individual *K* indices. The timeline for the calculation and distribution of *Kp* is analog to the timeline described for *K* in the paragraph above: With new data coming in, the *Kp* values get updated and once all data for the respective three-hour interval is available, *Kp* changes very little since only the determination of the quiet curve is affected by newly incoming data. The quiet curve is not changing any more once all data of the following day is available. However, late delivery of data from the *Kp* stations that fill in data gaps could retrospectively change our nowcast *Kp* values. Only with the monthly upload to the archive at GFZ Data Services (typically one week after the month in question, see section 4), the nowcast *Kp* values become fixed (even in the case of remaining data gaps). The calculation of nowcast *Kp* from nowcast *K* and *Ks* was slightly modified on August 1, 2020, and is described in the following paragraph.

We investigate differences between the nowcast and definitive *Kp* for 2019 by calculating the conditional and normalized occurrence of nowcast *Kp* given a certain definitive *Kp*. The normalization guarantees that the sum of all nowcast values for each definitive *Kp* amounts to 100%. For example, as shown in Figure 5a, for the condition of definitive *Kp* = 0o, there occurs a nowcast *Kp* = 0, 0+, and 1− in 73.2%, 26.1%, and 0.7% of the cases, respectively. Mostly, agreement between definitive and nowcast is around 70%. It is always above 55%, with the exception of *Kp* = 5−, where the nowcast *Kp* is underestimating the definitive *Kp* in 66% of the cases. Overall, the definitive and nowcast values differ mostly by one third of a unit, very rarely by two thirds (note the non-linear color scale in Figure 5a) and never by more than two thirds. A noteworthy discrepancy is seen for definitive *Kp* = 0o, where slightly more than 25% of nowcast *Kp* = 0+. There are two obvious reasons to explain the observed differences: First, the underlying NRT observatory data is preliminary, i.e., it can be incomplete (and some of our nowcast *Kp* products indicate the number of contributing observatories with available data), erroneous data might not be completely removed, and its calibration can be different from that of later data versions. Second, the FMI algorithm is used for all 13 stations when calculating nowcast *K*, whereas the observatory-dependent algorithms detailed in section 2.4.4 are used for calculating definitive *K*. To investigate the second effect, we calculate *Kp* from definitive geomagnetic observatory data from 1995 to 2017 using the FMI method for all stations and compare it to the definitive *Kp*. This FMI-based *Kp* frequency distribution (blue horizontal lines in Figure 5b) has 15% less *Kp* = 0 and 6% more *Kp* = 0+ than the definitive *Kp* (gray bars in Figure 5b). Also, it mostly overestimates the number of 0+ ≤ *Kp* < 3 and mostly underestimates the number of *Kp* ≥ 3o. This fits well to Figure 5c, where 31% of definitive *Kp* = 0 yield an FMI-based *Kp* = 0+. Also, around 3o ≤ *Kp* ≤ 6o, the FMI-based *Kp* tends to be one third of a unit smaller than definitive *Kp* in about 25%–30% of the cases (color code orange in Figure 5c) and one third of a unit larger in only about 10% of the cases (color code greenish).

As indicated by the similarity of Figures 5a and 5c, the larger part of the differences between definitive and nowcast *Kp* can be attributed to the FMI algorithm, and not to NRT data quality. To compensate this effect of the FMI algorithm on nowcast *Kp*, we slightly rescale the transformation from FMI-based *Ks* to *Kp* such that the distribution (red horizontal lines in Figure 5b) of the new rescaled FMI-based *Kp* follows more closely the distribution of the definitive *Kp* (gray bars). The details of rescaling are given in Table S4. Indeed, the rescaling improves the nowcast *Kp*, as confirmed by Figure 5d. In particular, only 23% of definitive *Kp* = 0 yield a rescaled FMI-based *Kp* = 0+ (as compared to 31% before rescaling). Also, the rescaled FMI-based *Kp* tends to be more equally distributed around the definitive *Kp* value in the region between 3o ≤ *Kp* ≤ 6o, with 15%–20% of the values (yellowish color in Figure 5c) being one third smaller or one third larger than the definitive *Kp*. This rescaled FMI-based *Kp* is produced and distributed as GFZ's nowcast *Kp* since August 1, 2020.

NOAA distributes a product resembling the nowcast *Kp* index and based on a subset of 8 of the 13 *Kp*-stations. The NOAA index is provided as a single-digit index, i.e., only full integer values are provided on a three-day plot (https://www.swpc.noaa.gov/products/planetary-k-index) and in files back to 1994 (ftp://ftp.swpc.noaa.gov/pub/indices/old_indices/). We also calculate a single-digit version of GFZ's nowcast *Kp* and compare it to the definitive *Kp* for 2019 in Figure 5e, while in Figure 5f, we compare the NOAA nowcast to the definitive *Kp* for 2019. Agreement with definitive *Kp* is usually better for the GFZ nowcast than for the
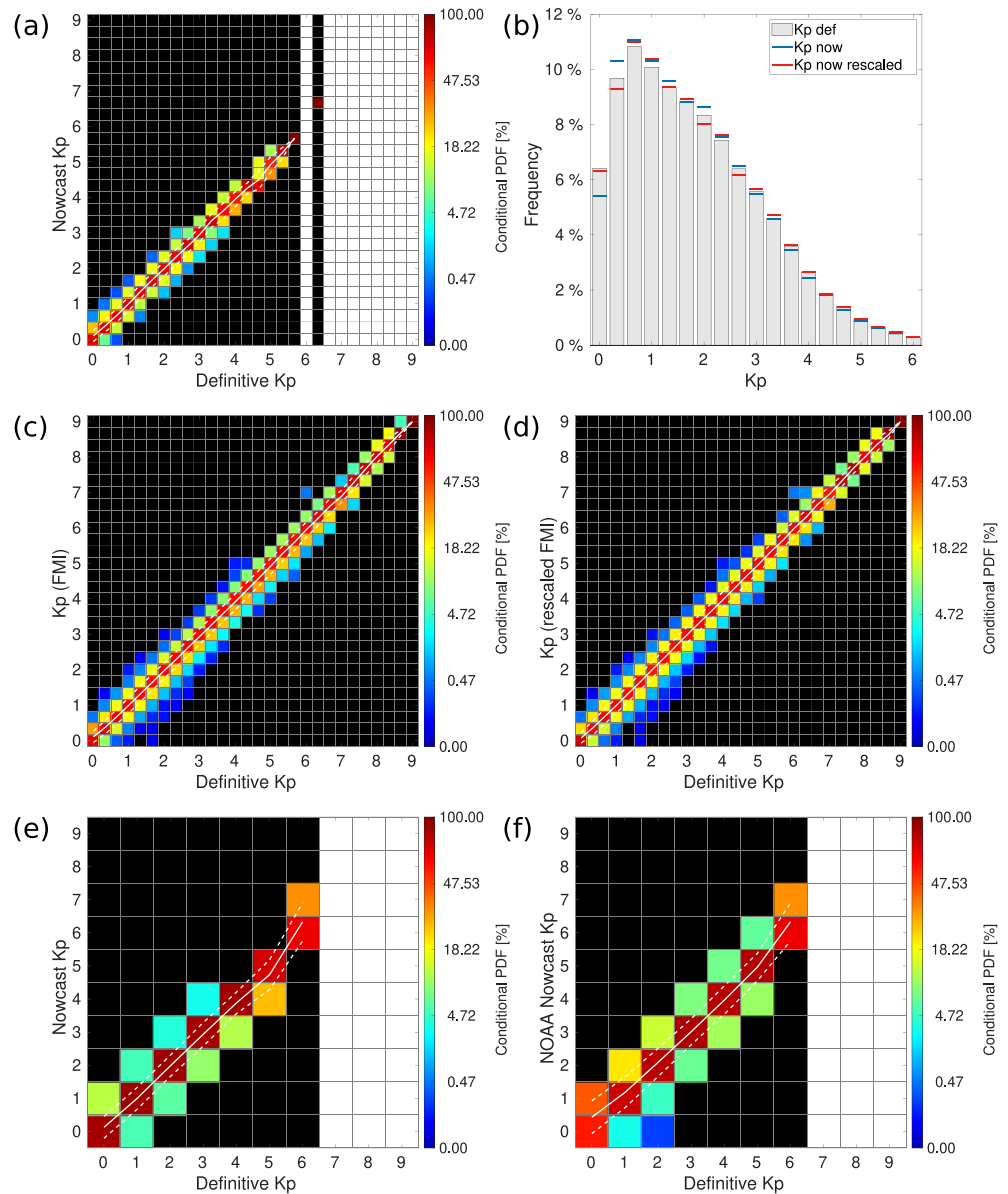
Figure 5. Comparison of nowcast and definitive *Kp*. (a) Normalized conditional occurrence of nowcast *Kp* for 2019. For a given value of the definitive *Kp* in 2019, the nowcast *Kp* distribution is shown color-coded and its mean and standard deviation are shown by white solid and dashed lines, respectively. (b) Frequency distribution of definitive *Kp*, FMI-based *Kp* (labeled *Kp* now), and rescaled FMI-based *Kp* (labeled *Kp* now rescaled) for 1995–2017 (data for *Kp* > 6 in Table S4). (c) Same as (a), but FMI-based *Kp* versus definitive *Kp* for 1995–2017. (d) Same as (c), but rescaled FMI-based *Kp*. (e) Same as (a), but values binned to single-digit *Kp* values. (f) Same as (e), but NOAA nowcast *Kp* versus definitive *Kp*. FMI, Finnish Meteorological Institute; NOAA, National Oceanic and Atmospheric Administration.

NOAA nowcast, except for Kp = 5, where NOAA and GFZ nowcast correctly predicted 83% and 73% of the cases. As for the GFZ nowcast, the NOAA product usually overestimates *Kp* = 0, with predicting values of 1 in 43% of the cases (12% for GFZ, and GFZs nowcast is further improved from August 2020 due to rescaling).

4. Distribution, DOI, License and Acknowledgment of *Kp*

Here, we discuss the distribution of *Kp*. An overview of the data distribution channels is given in Table S5 for GFZ and in Table S6 for data redistributors.

The DOI for *Kp* and the derived indices is 10.5880/Kp.0001. The DOI is a persistent identifier and while the data set grows with time, no value published under this DOI will ever be overwritten. If necessity arises in the future to correct already published values, then the corrected data set will be published with a new DOI (e.g., 10.5880/Kp.0002). Older DOIs and data sets will still be available. For each DOI, an additional versioning mechanism will be available to document changes to the files such as format changes, which do not affect the integrity of the data. The data set comprises *Kp*, *ap*, *Ap* (nowcast since 2019 and definitive since 1932, in WDC-format yearly ASCII files) and the *International Quiet and Disturbed Days* (table-like yearly ASCII-files). These data sets are updated on a monthly basis, typically one week after the end of the month. The DOI links to GFZ Data Services through https://doi.org/10.5880/Kp.0001, and this is the original data set to which all other copies must be identical, including the ones described in the following paragraph. More details are found in Table S5.

Another, traditional, source of the *Kp* index is the *Kp*-website of GFZ (https://www.gfz-potsdam.de/en/kp-index/). This page links to a number of data distribution services described in the following and in Table S5. The traditional *Kp* server (ftp://ftp.gfz-potsdam.de/pub/home/obs/kp-ap/) is updated half-monthly with definitive values and musical diagrams (also called "note-script", Bartels, 1949), and monthly and yearly with *Kp* frequency distributions and average *ap* values, respectively. In the WDC-format (format description on the FTP server), the *Kp*, *ap*, *Ap*, *CP* and *C*9 indices are accompanied by adjusted F10.7 values until 2006 and by sunspot numbers until 2014, when the new S_N sunspot number was introduced (Clette & Lefèvre, 2016). As a new service, we provide now SN9C9-plots with the new S_N sunspot number to replace the R9C9-plots. Sudden storm commencements (SSC, excluding sudden impulses, SI) are also listed and included in the musical diagrams. First, we use SSCs as detected at Niemegk observatory and, once available, replace these with the SSC list of the International Service on Rapid Magnetic Variations at Observatory Ebro (http://www.obsebre.es/en/rapid). The GFZ *Kp*-website also links to constantly updated digital and graphical nowcast values for the current and previous month, some indicating the number of stations available for the nowcast value, and a color-coded bar plot for the current and previous six days. A new service is an online generator and download function for this type of plots (as png, jpg, gif, eps, pdf) for dates back to January 1, 1932, with the most recent *Kp* values being nowcast values and earlier values being definitive values.

Another, new, source (ftp://ftp.gfz-potsdam.de/pub/home/obs/Kp_ap_Ap_SN_F107/) is meant to give experts and non-experts convenient, NRT capable access to a blend of the most current definitive and nowcast *Kp* indices and other relevant parameters. These files contain *Kp*, *ap*, *Ap*, the observed F10.7 (recommended for ionospheric and atmospheric studies), the adjusted F10.7 (recommended for solar studies), see Tapping (2013), and the international (daily total) sunspot number S_N introduced in 2015 (Clette & Lefèvre, 2016). The blank-separated file format is easy to read in by code or as spreadsheets. *Kp* values are given as float with three decimals (e.g., 0.667 instead of 0.7 or 1−) and, next to the date, a linear time scale in days since January 01, 1932 is given as well as Bartels rotations. Both the starting time and the mean time of each three-hour interval is given, as *Kp* represents geomagnetic disturbance over the three-hour interval and the time stamp indicating the center of the interval might be more useful for certain applications. Two file versions exist. One version contains all data from one day in one line. The other version contains only the data from one three-hour interval per line and provides only *Kp* and *ap*. Yearly files and a file containing all data since 1932 are updated daily. A file for the most recent 30 days is updated continuously to support NRT operations. The *Kp* and sunspot number data is a combination of definitive data when available and nowcast data otherwise and regularly updated to replace nowcast with definitive values.

The *Kp* data set is published under the CC BY 4.0 license. Non-commercial and commercial use and redistribution are permitted under the conditions of the license, making the *Kp* universally available and usable. One of the conditions is attribution by citing the data publication (Matzka et al., 2021) and the present publication and referring to the data source GFZ. Table S6 lists a number of data redistributors that redistribute the *Kp*, including the WDCs for Geomagnetism in Copenhagen and in Kyoto and NASA.

5. Summary and Conclusions

The *Kp* index and derived products have proven their usefulness for over 70 years and are particularly important for space weather research and services. A DOI (Matzka et al., 2021) and the CC BY 4.0 license secure the data set's integrity and its future scientific as well as societal usability.

We review the production of the definitive *Kp* and how it changed in its history. The frequency distribution and fundamental properties of *Kp* are demonstrated on data from 1932 to 2019 (see Table 1 and 3, Figure 3). We stress the importance of the subauroral location of *Kp*-stations and investigate the change in distance between the *Kp*-stations and the auroral oval due to geomagnetic secular variation and station relocation. This distance is estimated to have increased by 1.7° QD latitude since 1932 (Figure 4b), almost all of it due to secular variation, while station relocation is negligible here. This results in a bias of the *Kp* series toward smaller *Kp* values with time. We estimate this bias, which developed from 1932 to 2020, to be smaller than two thirds of a unit and likely to be in the order of one third of a unit.

We describe the production of the nowcast *Kp* at GFZ for the first time. The first estimate is issued as early as 35 min (before August 2020 it was >90 min) after the start of the respective three-hour interval and it is updated continuously with new data coming in. Also, since mid-August 2020, the nowcast *Kp* index is rescaled to better match the definitive values. It yields the correct definitive *Kp* index in 60% of the cases and we expect that the remaining 40% are now equally distributed between nowcast values being one third of a unit larger (20% of cases) and one third of a unit smaller (20% of the cases) than the definitive *Kp*.

Data Availability Statement

Geomagnetic data was partly taken from INTERMAGNET. The total sunspot number data are provided by Royal Observatory of Belgium, Brussels and can be downloaded from the SILSO website (http://sidc.be/silso/home). The solar wind data with one-minute time resolution were obtained from the NASA OMNI web database (http://omniweb.gsfc.nasa.gov/). The NOAA nowcast *Kp* values were taken from ftp://ftp.swpc.noaa.gov/pub/indices/old_indices/. The official *Kp* values used in this study are available at ftp://datapub.gfz-potsdam.de/download/10.5880.Kp.0001. Calculation of QD was facilitated by https://github.com/aburrell/apexpy.

References

Agapitov, O. V., Artemyev, A. V., Mourenas, D., Mozer, F. S., & Krasnoselskikh, V. (2015). Empirical model of lower band chorus wave distribution in the outer radiation belt. *Journal of Geophysical Research: Space Physics*, *120*, 10425–10442. https://doi.org/10.1002/2015JA021829

Akasofu, S.-I. (2003). Aurora. In MeyersR. A. (Eds.), Ed., *Encyclopedia of physical science and technology*. (3rd ed., pp. 793–803). Academic Press. ISBN 9780122274107 https://doi.org/10.1016/B0-12-227410-5/00045-4

Alken, P., Thébault, E., Beggan, C. D., Amit, H., Aubert, J., Baerenzung, J., et al. (2021). International geomagnetic reference field: The thirteenth generation. *Earth Planets and Space*, *73*, 49. https://doi.org/10.1186/s40623-020-01288-x

Bartels, J. (1938). Potsdamer erdmagnetische Kennziffern, 1. *Mitteilung. Zeitschrift f ür Geophysik*, *14*, 68–78. https://doi.org/10.23689/fidgeo-3165

Bartels, J. (1939). Potsdamer erdmagnetische Kennziffern, 4. *Mitteilung. Zeitschrift f ür Geophysik*, *15*, 214–221. https://doi.org/10.23689/fidgeo-3179

Bartels, J. (1949). The standardized index, Ks, and the planetary index, Kp. *IATME Bull.*, *12b*, 97–120.

Bartels, J. (1957a). The technique of scaling indices K and Q of geomagnetic activity. *Annals of the International Geophysical Year*, *4*, 215–226.

Bartels, J. (1957b). The geomagnetic measures for the time-variations of solar corpuscular radiation, described for use in correlation studies in other geophysical fields. *Annals of the International Geophysical Year*, *4*, 227–236. https://doi.org/10.1016/b978-1-4832-1304-0.50007-5

Bartels, J., Heck, N. H., & Johnston, H. F. (1939). The three-hour-range index measuring geomagnetic activity. *Journal of Geophysical Research*, *44*(4), 411–454. https://doi.org/10.1029/TE044i004p00411

Bartels, J., Heck, N. H., & Johnston, H. F. (1940). Geomagnetic three-hour-range indices for the years 1938 and 1939. *Journal of Geophysical Research*, *45*(3), 309–337. https://doi.org/10.1029/TE045i003p00309

Bartels, J., & Johnston, H. F. (1939). Main features of daily magnetic variations at Sitka, Cheltenham, Tucson, San Juan, Honolulu, Huancayo, and Watheroo. *Journal of Geophysical Research*, *44*, 455–469. https://doi.org/10.1029/TE044i004p00455

Berger, T. E., Holzinger, M. J., Sutton, E. K., & Thayer, J. P. (2020). Flying through uncertainty. *Space Weather*, *18*. https://doi.org/10.1029/2019SW002373

Boteler, D. H. (2001). Assessment of geomagnetic hazard to power systems in Canada. *Natural Hazards*, *23*, 101–120. https://doi.org/10.1023/A:1011194414259

Bruinsma, S. (2015). The DTM-2013 thermosphere model. *Journal of Space Weather and Space Climate*, *5*, A1. https://doi.org/10.1051/swsc/2015001

Chakraborty, S., & Morley, S. K. (2020). Probabilistic prediction of geomagnetic storms and the Kp index. *Journal of Space Weather and Space Climate*, *10*. https://doi.org/10.1051/swsc/2020037

Chapman, S., & Bartels, J. (1940). *Geomagnetism*. London: Oxford University Press.

Chulliat, A., Matzka, J., Masson, A., & Milan, S. E. (2017). Key ground-based and space-based assets to disentangle magnetic field sources in the Earth's environment. *Space Science Reviews*, *206*, 123–156. https://doi.org/10.1007/s11214-016-0291-y

Clark, T. D. G. (1992). Computer generated K indices adopted by the British Geological Survey. *Journal of Atmospheric and Terrestrial Physics*, *54*, 447–456. https://doi.org/10.1016/0021-9169(92)90023-E

Clette, F., & Lefèvre, L. (2016). The new sunspot number: Assembling all corrections. *Solar Physics*, *291*, 2629–2651. https://doi.org/10.1007/s11207-016-1014-y

Cliver, E. W., Kamide, Y., & Ling, A. G. (2000). Mountains versus valleys: Semiannual variation of geomagnetic activity. *Journal of Geophysical Research*, *105*, 2413–2424. https://doi.org/10.1029/1999JA900439

Cnossen, I., Richmond, A. D., & Wiltberger, M. (2012). The dependence of the coupled magnetosphere-ionosphere-thermosphere system on the Earth's magnetic dipole moment. *Journal of Geophysical Research*, *117*. https://doi.org/10.1029/2012JA017555

Curto, J. J., & Gaya-Piqué, L. R. (2009). Geoeffectiveness of solar flares in magnetic crochet (sfe) production: I-Dependence on their spectral nature and position on the solar disk. *Journal of Atmospheric and Solar-Terrestrial Physics*, *71*, 1695–1704. https://doi.org/10.1016/j.jastp.2008.06.018

Denton, M. H., Thomsen, M. F., Jordanova, V. K., Henderson, M. G., Borovsky, J. E., Denton, J. S., et al. (2015). An empirical model of electron and ion fluxes derived from observations at geosynchronous orbit. *Space Weather*, *13*, 233–249. https://doi.org/10.1002/2015SW001168

Emery, B. A., Coumans, V., Evans, D. S., Germany, G. A., Greer, M. S., Holeman, E., et al. (2008). Seasonal, Kp, solar wind, and solar flux variations in long-term single-pass satellite estimates of electron and ion auroral hemispheric power. *Journal of Geophysical Research - A: Space Physics*, *113*. https://doi.org/10.1029/2007JA012866

Emmert, J. T., Drob, D. P., Picone, J. M., Siskind, D. E., Jones, M., Mlynczak, M. G., et al. (2020). NRLMSIS 2.0: A whole atmosphere empirical model of temperature and neutral species densities. *Earth and Space Science*, *7*, e2020EA001321. https://doi.org/10.1029/2020EA001321

Emmert, J. T., Drob, D. P., Shepherd, G. G., Hernandez, G., Jarvis, M. J., Meriwether, J. W., et al. (2008). DWM07 global empirical model of upper thermospheric storm-induced disturbance winds. *Journal of Geophysical Research*, *113*. https://doi.org/10.1029/2008JA013541

Emmert, J. T., & Picone, J. M. (2010). Climatology of globally averaged thermospheric mass density. *Journal of Geophysical Research*, *115*. https://doi.org/10.1029/2010JA015298

Emmert, J. T., Richmond, A. D., & Drob, D. P. (2010). A computationally compact representation of Magnetic-Apex and Quasi-Dipole coordinates with smooth base vectors. *Journal of Geophysical Research*, *115*. https://doi.org/10.1029/2010JA015326

Fritz, H. (1881). *Das Polarlicht*, Leipzig: Brockhaus. https://doi.org/10.3931/e-rara-2131

Gussenhoven, M. S., Hardy, D. A., & Burke, J. W. (1981). DMSP/F2 electron observations of equatorward auroral boundaries and their relationship to magnetospheric electric fields. *Journal of Geophysical Research*, *86*, 768–778. https://doi.org/10.1029/JA086iA02p00768

Gussenhoven, M. S., Hardy, D. A., & Heinemann, N. (1983). Systematics of the equatorward diffuse auroral boundary. *Journal of Geophysical Research*, *88*, 5692–5708, https://doi.org/10.1029/JA088iA07p05692

Gustafsson, G., Papitashvili, N. E., & Papitashvili, V. O. (1992). A revised corrected geomagnetic coordinate system for Epochs 1985 and 1990. *Journal of Atmospheric and Terrestrial Physics*, *54*, 1609–1631. https://doi.org/10.1016/0021-9169(92)90167-J

Hardy, D. A., Gussenhoven, M. S., Raistrick, R., & McNeil, W. J. (1987). Statistical and functional representations of the pattern of auroral energy flux, number flux, and conductivity. *Journal of Geophysical Research*, *92*, 12275–12294. https://doi.org/10.1029/JA092iA11p12275

Hattingh, M., Loubser, L., & Nagtegaal, D. (1989). Computer K-index estimation by a new linear-phase, robust, non-linear smoothing method. *Geophysical Journal International*, *99*, 533–547. https://doi.org/10.1111/j.1365-246X.1989.tb02038.x

He, C., Yang, Y., Carter, B., Zhang, K., Hu, A., Li, W., et al. (2020). Impact of thermospheric mass density on the orbit prediction of satellites. *Space Weather*, *18*. https://doi.org/10.1029/2019SW002336

Heilig, B., & Lühr, H. (2013). New plasmapause model derived from CHAMP field-aligned current signatures. *Annales Geophysicae*, *31*, 529–539. https://doi.org/10.5194/angeo-31-529-2013

Horne, R. B., Glauert, S. A., Meredith, N. P., Boscher, D., Maget, V., Heynderickx, D., & Pitchford, D. (2013). Space weather impacts on satellites and forecasting the Earth's electron radiation belts with SPACECAST. *Space Weather*, *11*, 169–186. https://doi.org/10.1002/swe.20023

Jackson, D. R., Bruinsma, S., Negrin, S., Stolle, C., Budd, C. J., Dominguez Gonzalez, R., et al. (2020). The Space Weather Atmosphere Models and Indices (SWAMI) Project: Overview and first results. *Journal of Space Weather and Space Climate*, *10*, 18. https://doi.org/10.1051/swsc/2020019

Jordanova, V. K., Miyoshi, Y. S., Zaharia, S., Thomsen, M. F., Reeves, G. D., Evans, D. S., et al. (2006). Kinetic simulations of ring current evolution during the geospace environment modeling challenge events. *Journal of Geophysical Research - A: Space Physics*, *111*. https://doi.org/10.1029/2006JA011644

Kamide, Y., & Maltsev, Y. P. (2007). Geomagnetic storms. In Kamide, Y., & Chian, C.-L. (Eds.), Eds., *Handbook of the solar-terrestrial environment*. (pp. 355–374). Springer. ISBN 978-3-540-46315-3 https://doi.org/10.1007/978-3-540-46315-3_14

Kauristie, K., Morschhauser, A., Olsen, N., Finlay, C. C., McPherron, R. L., Gjerloev, J. W., & Opgenoorth, H. J. (2017). On the usage of geomagnetic indices for data selection in internal field modeling. *Space Science Reviews*, *206*, 61–90. https://doi.org/10.1007/s11214-016-0301-0

King, J. H., & Papitashvili, N. E. (2005). Solar wind spatial scales in and comparisons of hourly wind and ACE plasma and magnetic field data. *Journal of Geophysical Research*, *110*. https://doi.org/10.1029/2004JA010649

Korth, H., Thomsen, M. F., Borovsky, J. E., & McComas, D. J. (1999). Plasma sheet access to geosynchronous orbit. *Journal of Geophysical Research*, *104*, 25047–25061. https://doi.org/10.1029/1999JA900292

Kuvshinov, A. V. (2008). 3-D global induction in the oceans and solid Earth: Recent progress in modeling magnetic and electric fields from sources of magnetospheric, ionospheric and oceanic origin. *Surveys in Geophysics*, *29*, 139–186. https://doi.org/10.1007/s10712-008-9045-z

Laundal, K. M., & Richmond, A. D. (2017). Magnetic coordinate systems. *Space Science Reviews*, *206*, 27–59. https://doi.org/10.1007/s11214-016-0275-y

Lei, J., Thayer, J. P., Forbes, J. M., Sutton, E. K., & Nerem, R. S. (2008). Rotating solar coronal holes and periodic modulation of the upper atmosphere. *Geophysical Research Letters*, *35*. https://doi.org/10.1029/2008GL035208

Lei, J., Thayer, J. P., Forbes, J. M., Wu, Q., She, C., Wan, W., & Wang, W. (2008). Ionosphere response to solar wind high-speed streams. *Geophysical Research Letters*, *35*. https://doi.org/10.1029/2008GL033875

Liu, H.-L., Bardeen, C. G., Foster, B. T., Lauritzen, P., Liu, J., Lu, G., et al. (2018). Development and validation of the Whole Atmosphere Community Climate Model with Thermosphere and Ionosphere extension (WACCM-X 2.0). *Journal of Advances in Modeling Earth Systems*, *10*, 381–402. https://doi.org/10.1002/2017MS001232

Lockwood, M., Stamper, R., & Wild, M. N. (1999). A doubling of the Sun's coronal magnetic field during the past 100 years. *Nature*, *399*, 437–439. https://doi.org/10.1038/20867

Manoj, C., Maus, S., Lühr, H., & Alken, P. (2008). Penetration characteristics of the interplanetary electric field to the daytime equatorial ionosphere. *Journal of Geophysical Research*, *113*. https://doi.org/10.1029/2008JA013381

Matzka, J., Bronkalla, O., Tornow, K., Elger, K., & Stolle, C. (2021). *Geomagnetic Kp index. V. 1.0.* GFZ Data Services. https://doi.org/10.5880/Kp.0001

Matzka, J., Chulliat, A., Mandea, M., Finlay, C. C., & Qamili, E. (2010). Geomagnetic observations for main field studies: From ground to space. *Space Science Reviews*, *155*, 29–64. https://doi.org/10.1007/s11214-010-9693-4

Matzka, J., Pedersen, L. W., Fox Maule, C., Neska, A., Reda, J., Nilsson, A., & Linthe, H.-J. (2009). The effect of high voltage DC power lines on the geomagnetic measurement at BFE. In J. J. Love (Ed.), Ed., *Proceedings of the XIII. IAGA Workshop on geomagnetic observatory instruments, data acquisition, and processing.* (pp. 162–170). US Geological Survey Open-File Report 2009-1226.

Maule, C. F., Thejll, P., Neska, A., Matzka, J., Pedersen, L. W., & Nilsson, A. (2009). Analyzing and correcting for contaminating magnetic fields at the Brorfelde geomagnetic observatory due to high voltage DC power lines. *Earth, Planets and Space*, *61*, 1233–1241. https://doi.org/10.1186/BF03352976

Maus, S., & Lühr, H. (2005). Signature of the quiet-time magnetospheric magnetic field and its electromagnetic induction in the rotating Earth. *Geophysical Journal International*, *162*, 755–763. https://doi.org/10.1111/j.1365-246X.2005.02691.x

Mayaud, P. N. (1980). Derivation, meaning, and use of geomagnetic indices. *Geophysical Monograph Series*, *22*. American Geophysical Union, ISBN:9780875900223 https://doi.org/10.1029/GM022

McGranaghan, R. M., Mannucci, A. J., Wilson, B., Mattmann, C. A., & Chadwick, R. (2018). New capabilities for prediction of high-latitude ionospheric scintillation: A novel approach with machine learning. *Space Weather*, *16*, 1817–1846. https://doi.org/10.1029/2018SW002018

McIlwain, C. E. (1986). A Kp dependent equatorial electric field model. *Advances in Space Research*, *6*, 187–197. https://doi.org/10.1016/0273-1177(86)90331-5

McNoe, P. A. (1989). *Use of inclination in the automatic derivation of geomagnetic K-indices*, Exeter, UK: Oral presentation at the 6th IAGA Scientific Assembly.

McPherron, R. L., & Chu, X. (2017). The mid-latitude positive bay and the MPB index of substorm activity. *Space Science Reviews*, *206*, 91–122. https://doi.org/10.1007/s11214-016-0316-6

Menvielle, M. (1981). About the scalings of K indices. *IAGA News*, *20*, 110–111.

Menvielle, M., & Berthelier, A. (1991). The K-derived planetary indices: Description and availability. *Reviews of Geophysics*, *29*, 415–432. https://doi.org/10.1029/91RG00994

Menvielle, M., Papitashvili, N., Hakkinen, L., & Sucksdorff, C. (1995). Computer production of K indices: review and comparison of methods. *Geophysical Journal International*, *123*, 866–886. https://doi.org/10.1111/j.1365-246X.1995.tb06895.x

Newell, P. T., Sotirelis, T., Liou, K., Meng, C. I., & Rich, F. J. (2007). A nearly universal solar wind-magnetosphere coupling function inferred from 10 magnetospheric state variables. *Journal of Geophysical Research: Space Physics*, *112*. https://doi.org/10.1029/2006JA012015

Nowozynski, K., Ernst, T., & Jankowski, J. (1991). Adaptive smoothing method for computer derivation of K-indices. *Geophysical Journal International*, *104*, 85–93. https://doi.org/10.1111/j.1365-246X.1991.tb02495.x

O'Brian, T. P., & Moldwin, M. B. (2003). Empirical plasmapause models from magnetic indices. *Geophysical Research Letters*, *30*. https://doi.org/10.1029/2002GL016007

Oguti, T. (1993). Prediction of the location and form of the auroral zone: Wandering of the auroral zone out of high latitudes. *Journal of Geophysical Research*, *98*, 11649–11655. https://doi.org/10.1029/93JA00328

Ozeke, L. G., Mann, I. R., Murphy, K. R., Jonathan Rae, I., & Milling, D. K. (2014). Analytic expressions for ULF wave radiation belt radial diffusion coefficients. *Journal of Geophysical Research: Space Physics*, *119*, 1587–1605. https://doi.org/10.1002/2013JA019204

Pierrard, V., Goldstein, J., André, N., Jordanova, V. K., Kotova, G. A., Lemaire, J. F., et al. (2009). Recent progress in physics-based models of the plasmasphere. *Space Science Reviews*, *145*, 193–229. https://doi.org/10.1007/s11214-008-9480-7

Pierrard, V., & Stegen, K. (2008). A three-dimensional dynamic kinetic model of the plasmasphere. *Journal of Geophysical Research - A: Space Physics*, *113*. https://doi.org/10.1029/2008JA013060

Qian, L., Burns, A. G., Emery, B. A., Foster, B., Lu, G., Maute, A., et al. (2014). The NCAR TIE-GCM: A community model of the coupled thermosphere/ionosphere system. In Huba, J., Schunk, R., & Khazanov, G. (Eds.), Eds., *Modeling the ionosphere-thermosphere system*, (p. 201). AGU Geophysical Monograph Series. https://doi.org/10.1002/9781118704417.ch7

Rangarajan, G. K. (1987). Indices of geomagnetic activity. In Jacobs, J. A. (Ed.), Ed., *Geomagnetism, 3*. (pp. 323–384). Academic Press.

Russell, C. T., Luhmann, J. G., & Jian, L. K. (2010). How unprecedented a solar minimum? *Reviews of Geophysics*, *48*, RG2004. https://doi.org/10.1029/2009RG000316

Russell, C. T., & McPherron, R. L. (1973). Semiannual variation of geomagnetic activity. *Journal of Geophysical Research*, *78*, 92–108. https://doi.org/10.1029/JA078i001p00092

Secan, J. A., Bussey, R. M., Fremouw, E. J., & Basu, S. (1997). High-latitude upgrade to the wideband ionospheric scintillation model. *Radio Science*, *32*(4), 1567–1574. https://doi.org/10.1029/97RS00453

Shprits, Y. Y., Meredith, N. P., & Thorne (2007). Parameterization of radiation belt electron loss time scales due to interaction with chorus waves. *Geophysical Research Letters*, *34*. https://doi.org/10.1029/2006GL029050

Shprits, Y. Y., Vasile, R., & Zhelavskaya, I. S. (2019). Nowcasting and predicting the Kp index using historical values and real-time observations. *Space Weather*, *17*, 1219–1229. https://doi.org/10.1029/2018SW002141

Siebert, M. (1971). Maßzahlen der erdmagnetischen Aktivität. In Rawer, K. (Ed.), Ed., *Encyclopedia of physics/Handbuch der Physik*. (pp. 206–275). Berlin Heidelberg, New York: Springer.

Siebert, M., & Meyer, J. (1996). Geomagnetic activity indices. In Dieminger, W., Hartmann, W., & Leitinger, G. K. (Eds.), Eds., *The upper atmosphere*. (pp. 887–911). Berlin Heidelberg: Springer.

Smith, A. R. A., Beggan, C. D., Macmillan, S., & Whaler, K. A. (2017). Climatology of the auroral electrojets derived from the along-track gradient of magnetic field intensity measured by POGO, Magsat, CHAMP, and Swarm. *Space Weather*, *15*, 1257–1269. https://doi.org/10.1002/2017SW001675

St-Louis, B. (2012). *INTERMAGNET technical reference manual, V 4.6*. INTERMAGNET Operations Committee and Executive Council. https://www.intermagnet.org/publications/intermag_4-6.pdf

Subbotin, D. A., Shprits, Y. Y., & Ni, B. (2011). Long-term radiation belt simulation with the VERB 3-D code: Comparison with CRRES observations. *Journal of Geophysical Research*, *116*. https://doi.org/10.1029/2011JA017019

Sucksdorff, C., Pirjola, R., & Häkkinen, L. (1991). Computer production of K-indices based on linear elimination. *Geophysical Transactions*, *36*, 333–345. https://epa.oszk.hu/02900/02941/00076/pdf/EPA02941_geofizikai_kozlemenyek_1991_36_3-4_321-332.pdf

Svalgaard, L. (1976). Recalibration of Bartels' geomagnetic activity indices Kp and ap to include universal time variations. *Journal of Geophysical Research*, *81*, 5182–5188. https://doi.org/10.1029/JA081i028p05182

Takahashi, K., Toth, B. A., & Olson, J. V. (2001). An automated procedure for near-real-time Kp estimates. *Journal of Geophysical Research*, *106*(A10), 21017–21032. https://doi.org/10.1029/2000JA000218

Tapping, K. F. (2013). The 10.7 cm solar radio flux (F10.7). *Space Weather*, *11*, 394–406. https://doi.org/10.1002/swe.20064

Thomsen, M. F. (2004). Why Kp is such a good measure of magnetospheric convection. *Space Weather*, *2*, S11004. https://doi.org/10.1029/2004SW000089

Tsyganenko, N. A. (1989). A magnetospheric magnetic field model with a warped tail current sheet. *Planetary and Space Science*, *37*, 5–20. https://doi.org/10.1016/0032-0633(89)90066-4

Veldkamp, J., & van Sabben, D. (1960). On the current system of solar-flare effects. *Journal of Atmospheric and Terrestrial Physics*, *18*, 192–202. https://doi.org/10.1016/0021-9169(60)90092-1

Wilson, L. R. (1987). An evaluation of digitally derived K-indices. *Journal of Geomagnetism and Geoelectricity*, *39*, 97–109. https://doi.org/10.5636/jgg.39.97

Wing, S., Johnson, J. R., Jen, J., Meng, C. I., Sibeck, D. G., Bechtold, K., & Takahashi, K. (2005). Kp forecast models. *Journal of Geophysical Research*, *110*. https://doi.org/10.1029/2004JA010500

Wintoft, P., Wik, M., Matzka, J., & Shprits, Y. (2017). Forecasting Kp from solar wind data: Input parameter study using 3-hour averages and 3-hour range values. *Journal of Space Weather and Space Climate*, *7*, A29. https://doi.org/10.1051/swsc/2017027

Workayehu, A. B., Vanhamäki, H., & Aikio, A. T. (2019). Field-Aligned and Horizontal Currents in the Northern and Southern Hemispheres from the Swarm satellite. *Journal of Geophysical Research: Space Physics*, *124*, 7231–7246. https://doi.org/10.1029/2019JA026835

Xiong, C., Lühr, H., Wang, H., & Johnsen, M. G. (2014). Determining the boundaries of the auroral oval from CHAMP field-aligned current signatures - Part 1. *Annales Geophysicae*, *32*, 609–622. https://doi.org/10.5194/angeo-32-609-2014

Xiong, C., Stolle, C., & Lühr, H. (2016). The Swarm satellite loss of GPS signal and its relation to ionospheric plasma irregularities. *Space Weather*, *14*(8), 563–577. https://doi.org/10.1002/2016SW001439

Xiong, C., Stolle, C., & Park, J. (2018). Climatology of GPS signal loss observed by Swarm satellites. *Annales Geophysicae*, *36*, 679–693. https://doi.org/10.5194/angeo-36-679-2018

Yamazaki, Y., & Maute, A. (2017). Sq and EEJ-A Review on the daily variation of the geomagnetic field caused by ionospheric dynamo currents. *Space Science Reviews*, *206*, 299–405. https://doi.org/10.1007/s11214-016-0282-z

Yau, A. W., Peterson, W. K., & Abe, T. (2011). Influences of the ionosphere, thermosphere and magnetosphere on ion outflows. In Liu, W., & Fujimoto, M. (Eds.), Eds., *The dynamic magnetosphere*. (pp. 283–314). Dordrecht: Springer Netherlands. https://doi.org/10.1007/978-94-007-0501-2_16

Zhang, Y., & Paxton, L. J. (2008). An empirical Kp-dependent global auroral model based on TIMED/GUVI FUV data. *Journal of Atmospheric and Solar-Terrestrial Physics*, *70*, 1231–1242. https://doi.org/10.1016/j.jastp.2008.03.008

Zhelavskaya, I., Shprits, Y., & Spasojević, M. (2017). Empirical modeling of the plasmasphere dynamics using neural networks. *Journal of Geophysical Research - A: Space Physics*, *122*, 11227–11244. https://doi.org/10.1002/2017JA024406

Zhelavskaya, I. S., Vasile, R., Shprits, Y. Y., Stolle, C., & Matzka, J. (2019). Systematic analysis of machine learning and feature selection techniques for prediction of the Kp index. *Space Weather*, *17*, 1461–1486. https://doi.org/10.1029/2019SW002271